DEVELOPMENT OF OPTICAL FIBER SENSORS FOR DISTANCE, REFRACTIVE INDEX AND STRAIN MEASUREMENT

by

AYAN MAJUMDAR

Presented to the Faculty of the Graduate School of

The University of Texas at Arlington in Partial Fulfillment

of the Requirements

for the Degree of

MASTER OF SCIENCE IN MECHANICAL ENGINEERING

THE UNIVERSITY OF TEXAS AT ARLINGTON

December 2008

To my Dad

ACKNOWLEDGEMENTS

I would like to express my heartfelt gratitude to my mentor, Dr.Haiying Huang, for her generous support throughout the course of my study as well as research. She shared a lot of her expertise and technical insights with me, which have taught me innumerable lessons in academic research. I am especially grateful to her for her faith in me, refusing to accept anything less than the best that I could do. With her dedication, confidence, and determination, she will continue to remain my mentor for the journey ahead.

I would like to thank Dr. Frank Lu and Dr. Brian Dennis for taking time out and agreeing to be on my thesis defense committee. I would also like to thank Gonzalo Amador for allowing me to work on my thesis during my internship and giving me valuable advice. I also would like to extend my gratitude to all my friends, especially Chirag, Vinayak and Kavita for patiently listening to me vent my frustration when I have been stuck with this thesis, although they did not understand a word of what I was saying.

Words are too little to express my gratitude and love to my parents for providing me with this opportunity and constantly encouraging me throughout. I would especially like to thank my father for having insane amounts of faith in me and inspiring me to reach greater heights. To him I dedicate this thesis.

October 6, 2008.

ABSTRACT

DEVELOPMENT OF OPTICAL FIBER SENSORS TO DISTANCE, REFRACTIVE INDEX AND STRAIN MEASUREMENT

Ayan Majumdar, M.S.

The University of Texas at Arlington, 2008

Supervising Professor: Haiying Huang

Optical fiber based sensing techniques provide a unique set of sensors which are small, lightweight, immune to EMI, easily multiplexed, and in most cases, inexpensive to manufacture. These advantages are the motivation behind continued research and development in this field. This thesis is focused on the development of optical fiber based sensors for the measurement of distance, refractive index, and strain. The fabrication, implementation, analysis, and evaluation of the sensors are presented.

The Extrinsic Fabry-Perot Interferometric (EFPI) distance sensor is one of the most popular distance sensors but it possesses an inherent drawback. When the free-space cavity distance is very small, the numbers of fringes generated are not sufficient for the distance demodulation algorithm; therefore the smallest distance it can measure is determined by the bandwidth of the light source. An optical fiber based distance sensor is developed in this thesis which is capable of overcoming this shortcoming by taking advantage of the mode coupling effect of a Long Period Fiber Grating (LPFG). The optical path difference (OPD) is contributed

by the free-space cavity distance as well as the LPFG cavity distance; therefore it can generate sufficient fringes even when the free space cavity distance is very small. A sensor probe with a metallic coating over its cladding region only is fabricated and a mechanically induced LPFG is implemented. The performance of the sensor is evaluated. It is confirmed that the LPFG-based distance sensor is capable of measuring distances as small as 4 microns which is significantly smaller than that can be measured by an EFPI sensor. A compact polymer tip based distance sensor is subsequently developed to overcome the shortcomings of the LPFG. The sensor consists of a polymer core fabricated at the end of the optical fiber. Similar to the LPFG based distance sensor, the OPD for this sensor is contributed by the free-space cavity distance as well as the phase shift introduced by the polymer core which helps it generate sufficient fringes for the distance demodulation.

The sensor probe fabricated for the polymer tip based distance sensor is extended to refractive index measurement by submerging the polymer core in the liquid whose refractive index needs to be measured. The effective refractive index of the polymer core changes with the external refractive index, producing a phase shift in the interference spectrum. In order to understand the performance of the refractive index sensor, a simulation model is developed. This simulation model is subsequently validated by the experimental data. A high sensitivity of 0.6 nm in fringe shift for every 0.01 change in refractive index is achieved experimentally when the sensor is immersed in different refractive index standards. The sensor also shows a 60% increase in sensitivity when compared with similar LPFG or interferometry-based refractive index sensors.

A strain sensor that is capable of measuring large strains is also developed by fabricating a polymer sensing element between two multi-mode fibers, using the sample polymer core fabrication process. It is experimentally validated that a strain as large as 56% can be measured using this hybrid glass/polymer sensor. The work to be done in the future in order to make these sensors commercially viable is also discussed.

TABLE OF CONTENTS

LIST OF ILLUSTRATIONS

Figure Page

CHAPTER 1

INTRODUCTION

1.1. Optical Fiber Sensors

Optical fiber sensors have been widely used to measure a range of parameters including refractive index, distance, concentration, strain, and humidity [1-4], just to name a few. Their versatile nature is mainly attributed to the unique set of advantages that they offer like light weight, compactness, ability to work in a harsh environment, and immunity to electromagnetic interference.

Optical fiber sensors can be classified in various ways but, often, the measurement scheme is chosen as the main criterion for classification. Optical fiber sensors based on measurement schemes are divided into two broad categories: intensity-based and wavelength-based. Wavelength-based sensors measure the physical parameter based on its influence on the wavelength of light. Intensity-based sensors, on the other hand, measure parameters based on the effect of the physical parameter on the intensity of either the reflected or transmitted light. Each category of sensors provides a unique set of advantages.

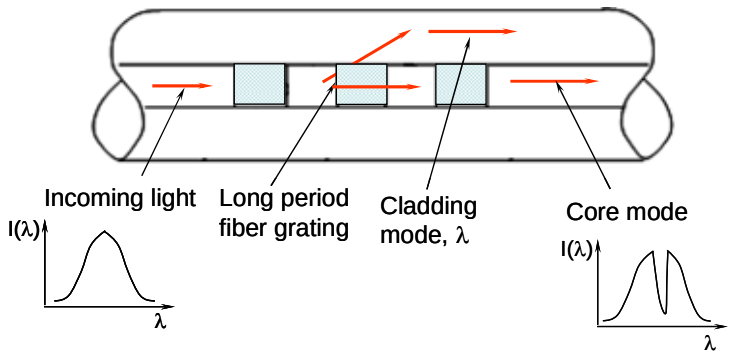

Figure 1.1 Long Period Fiber Grating

1.1.1 Wavelength-based vs. Intensity-based measurement schemes

In a wavelength-based measurement scheme, the sensitivity to any parameter is recorded as a change in the wavelength domain. A Long Period Fiber Grating (LPFG) based sensor is an example of a wavelength-based sensor. LPFGs are essentially periodic perturbations in the effective index of the optical fiber which couple a part of light into the cladding of the optical fiber, as shown in Figure 1.1. The period between the perturbations as well as the effective refractive index decides the wavelength at which this coupling takes place [5]. The light traveling in the core of the fiber, denoted as the core mode, displays a resonance loss at a particular wavelength when its intensity is plotted on the wavelength scale. This is the wavelength at which a part of the core mode is coupled out to the cladding mode. Various physical changes in the region surrounding the LPFG such as refractive index, strain, and temperature etc., can cause a shift in this wavelength, leading to a shift in the resonance loss observed on the wavelength scale. As a result, LPFG can serve as a very effective wavelength-based sensor. In addition, the beam splitting action of the LPFG allows it to be used as an interferometer. This application is described in detail in Chapter 2.

Intensity-based sensors, on the other hand, record the sensitivity to any parameter as a change in the intensity of light. Figure 1.2 gives an example of a strain sensor which employs an intensity-based measurement scheme [6]. As strain is applied, the distance between the two

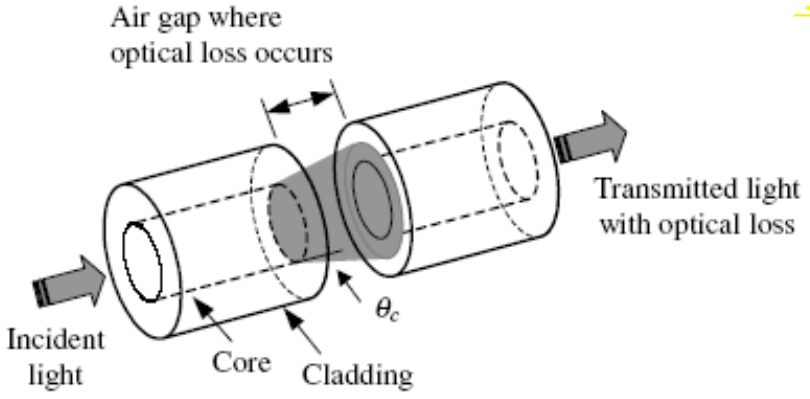

Figure 1.2 Strain sensor using a Intensity-based measurement scheme.[6]

fibers increases which in turn increases the optical loss, resulting in a reduction in the intensity of the transmitted light. The amount of strain applied can be easily correlated to the reduction in the intensity using this intensity-based measurement scheme.

From the examples given previously, it is evident that a wavelength-based measurement scheme requires a significant amount of data processing to determine the change in wavelength or the change in phase as compared to an intensity-based measurement scheme which requires minimal data processing and is therefore easier to implement. However most intensity-based measurement schemes require a reference signal in order to compare the reduction in intensity. This is a major drawback since generating a reference signal can add to the cost and the complexity of the sensor.

These two measurement schemes also differ in terms of accuracy and resolution; wavelength-based sensors such as LPFG offer high accuracy and ultra-high resolution. In comparison, intensity-based sensors are highly sensitive to environmental factors such as noise, bending loss etc. Therefore the choice of measurement scheme is critical in the successful functioning of the sensor. Often the choice is made based on the parameter to be measured as well as the range and accuracy desired. For the purpose of this thesis, only wavelength-based sensors are discussed.

1.2. Distance Measurement

Of the various parameters that can be measured using optical fiber sensors, distance measurement is perhaps the most important since it can be used for the measurement of other parameters such as pressure, strain etc. [7,8].

1.2.1 Whitelight Extrinsic Fabry-Perot Interfermetric (EFPI) Distance Sensor

Whitelight Interferometric (WLI) distance sensors, a wavelength-based measurement scheme, is one of the most popular optical fiber distance sensors. Whitelight is a combination of a broadband light spectrum produced by an incoherent source. Therefore, whitelight interferometric distance sensors can demodulate the absolute distance values from the

interference fringe positions over the wavelength scale and thus overcome the requirement of a reference signal.

Fabry-Perot interferometric sensors are the most popular whitelight interferometric sensors, among which the Extrinsic Fabry-Perot Interferometric (EFPI) sensor is the most common technique since it is flexible and easy to implement. A basic diagram for the EFPI as

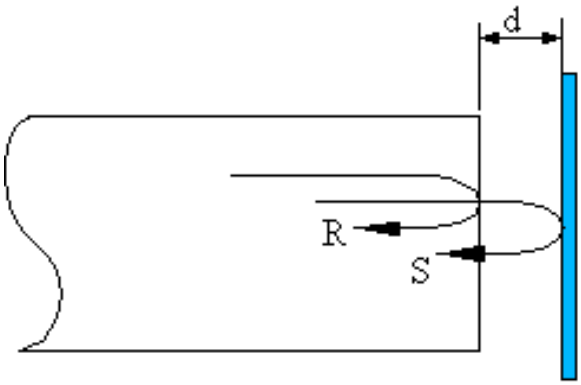

Figure 1.3 Basic diagram of EFPI as used in distance measurement**.**

used in distance measurement is shown in Fig.1.3. An optical fiber is placed in front of a target. The distance *d* between the optical fiber and the target is the parameter we want to measure.

When light traveling inside the optical fiber encounters the end surface of the optical fiber, some light is reflected at this core-air interface (R) due to the difference in the refractive index of the fiber core and the medium surrounding the fiber. The transmitted light is reflected off the surface of the target (S) after it travels the distance *d*. Thus S travels a longer optical distance than R and contains phase information regarding the distance between the end face of the optical fiber and the surface of the target. An interference pattern is generated due to the optical path difference (OPD) between the two. The interference pattern of frequency f_s is given by

$$I(d) = I_r + I_s + 2\sqrt{I_r I_s}\cos(2\pi f_s k + \theta), \tag{1.1}$$

where *k* is the wavenumber given by the inverse of the wavelength λ. Thus the interference can be seen as a sinusoidal pattern on the wavelength scale. The frequency, $f_{s,}$ is directly related to the OPD i.e, f_s=*OPD*. The optical distance is given by

$$OPD = n_m L, \tag{1.2}$$

where *L* is the difference in the distance traveled by two interfering beams. Therefore the OPD between R and S is

$$OPD = 2n_m d\ , \tag{1.3}$$

where n_m is the refractive index of the medium between the optical fiber and the sample surface and *d* is the distance of the sample surface from the optical fiber. It is twice since light gets reflected off the mirror and therefore travels the distance *d* twice. Thus, equation (1.1) can be rewritten as

$$I(d) = I_r + I_s + 2\sqrt{I_r I_s}\cos(4\pi n_m d/\lambda + \theta). \tag{1.4}$$

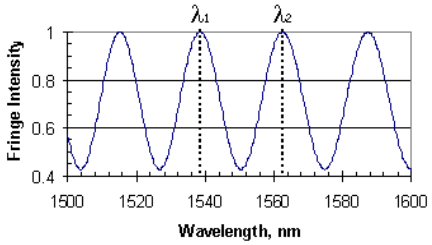

Figure 1.4 Normalized fringe pattern from a WLI distance sensor

From equation (4), it can be seen that the spacing and the location of the peaks and valleys, i.e., the fringes, are determined by the distance *d* and an unknown phase shift, assuming the sensor is operating in air. Figure 1.4 shows the normalized fringe spectrum of a FPI sensor. A large value of *d* would result in a high frequency which in turn would produce more fringes within a given wavelength range. As the distance *d* reduces, the frequency reduces which in turn increases the spectral spacing between the fringes. Since the distance *d* can be calculated from the positions of two adjacent fringes, e.g. λ_1 and λ_2,

$$d = \frac{\lambda_1 \lambda_2}{2n_m(\lambda_2 - \lambda_1)}, \tag{1.5}$$

it requires the presence of at least two fringes within the bandwidth of the whitelight source in order to measure the distance *d*. This imposes a limit on how small a distance a whitelight FPI distance sensor can measure. In addition, since an FPI sensor cannot measure temperature independently, it cannot account for temperature induced distance fluctuations. These limitations severely limit the applications of the WLI based distance sensor for Near-Field Surface profiling.

Near field surface profiling using a Near-field Scanning Optical Microscope (NSOM) is a very useful technique for the optical investigation of materials in the sub-wavelength range, particularly in the nano/bio applications [9]. A NSOM positions a tapered optical fiber probe in the near-field surface of the sample and thus overcomes the diffraction limit of conventional optical microscopes. However, the technique's further advancement, especially in the fields of biology and surface chemistry, is hindered due to its position feedback mechanism [10]. Moreover, despite a variety of light collecting techniques in NSOM, the basic image construction technique is solely dependent on measuring the intensity of the sample light using a photomultiplier tube. Therefore, its signal is susceptible to noises induced by laser power fluctuation and optical fiber bending. A WLI distance sensor that can conduct surface profiling in the near-field of the sample surface has obvious advantages because its capability for ultra-precise absolute distance measurement can be exploited for position feedback as well as for surface profiling. However, in order for a WLI distance sensor to be applicable for near-field surface profiling, it must have the capability of measuring distances as small as a few tens of nanometers, a requirement that cannot be satisfied by existing optical fiber-based WLI distance sensing techniques.

1.3. Objectives

The objectives of the work is to develop an optical fiber distance sensor that overcomes the distance limit of the whitelight EFPI distance measurement technique while still maintaining the simplicity and accuracy of the EFPI distance sensor.

The advantages of the proposed sensor are:

1) Capability of measuring very small distances – This is a huge advantage especially in the field of Near-Field Surface Profiling where distances are often measured on the nanometer scale using an expensive tapered optical fiber probe and a position feedback mechanism.

2) Absolute Distance Measurement - Absolute distance measurement helps remove the need for a position feedback mechanism and therefore makes the measurement system a lot simpler.

3) Capability of measuring Temperature and Distance simultaneously – Since the sensor will be capable of measuring temperature and distance simultaneously it can be used to account for temperature induced fluctuations in distance measurement, thus providing temperature-insensitive distance measurement. The performance of the sensor is not characterized for temperature induced distance fluctuations in this thesis.

4) Manufacturing technique can be exploited for fabricating other sensor probes – The simplicity of proposed manufacturing technique also gives us the opportunity to use it to fabricate sensor probes for measuring other important parameters such as refractive index and strain. This aspect of the sensor has been explored in this thesis.

1.4. Thesis Outline

In this thesis, the application of optical fiber sensors to the measurement of three main parameters is dicussed: distance, refractive index, and strain. Chapters 2 and 3 discuss the development of two different kinds of distance sensors that can overcome the distance limit of the EFPI distance sensor. Expanding the fabrication technique developed for the distance sensors to fabricate the sensor probes that measure refractive index and strain are discussed in Chapters 4 and 5. A summary of the sensors developed and the work to be done in the future is discussed in Chapter 6.

CHAPTER 2

LPFG-BASED OPTICAL FIBER SENSOR FOR ARBITRARY SMALL DISTANCE MEASUREMENT

The LPFG discussed in Chapter 1 is used to develop a distance sensor which overcomes the distance limit of the EFPI distance sensor. The fabrication technique, experimental setup and the results are described in this chapter.

2.1. Long Period Fiber Grating (LPFG)

As discussed before, LPFGs (Figure 1.1) are periodic perturbations in the effective index of the fiber which couple a part of light from the fiber core into the cladding of the optical fiber.

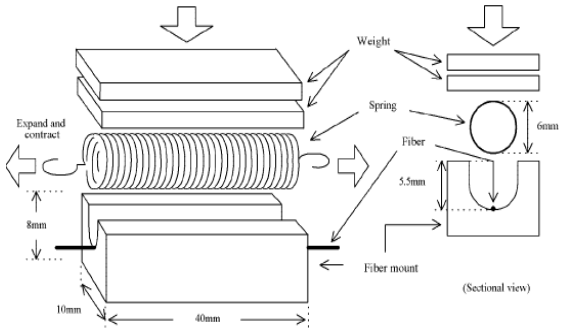

(a)

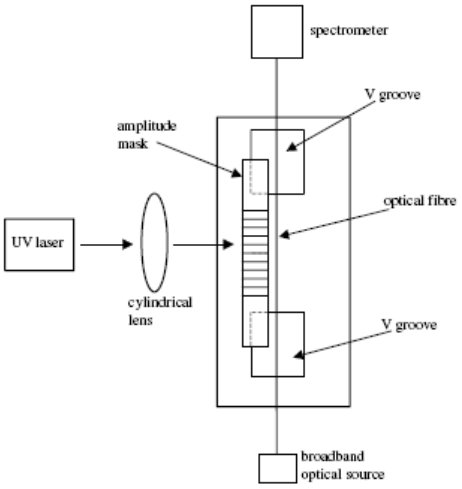

(b)

Figure 2.1 a) Mechanically Induced LPFG [12] b) LPFG using a UV laser [11]

The wavelength of the light that gets coupled into the cladding depends on the period of the perturbations, which typically varies between 100-1000 μm [5]. LPFGs are generally fabricated by applying high-power UV light through an amplitude photo-mask placed over the fiber via a cylindrical lens (see Figure 2.1b)[11]. Although such LPFGs are robust in performance, they are not flexible and at times quite expensive to manufacture. Mechanically-induced LPFGs on the other hand are flexible and inexpensive. By pressing a spring onto an optical fiber, a grating can be inscribed onto the fiber which has the same period of perturbation as that of the pitch of the spring. By stretching the spring the period of the perturbation can be changed (see Figure 2.1 a) [12].

2.2. Arbitrary Small Distance Measurement

2.2.1. Principle of Operation

An LPFG based WLI distance sensor setup is shown in Figure 2.2. It consists of a broadband source, an optical circulator, a distance sensor and an Optical Spectrum Analyzer (OSA). The light generated by the broadband source is routed towards the distance sensor probe by the optical circulator. The sensor probe, as shown in Figure 2.3 is simply a cladding coated Single Mode Fiber (SMF) with a LPFG located a distance from the cleaved end. The core mode keeps traveling along the fiber toward the sample under test, as indicated by the

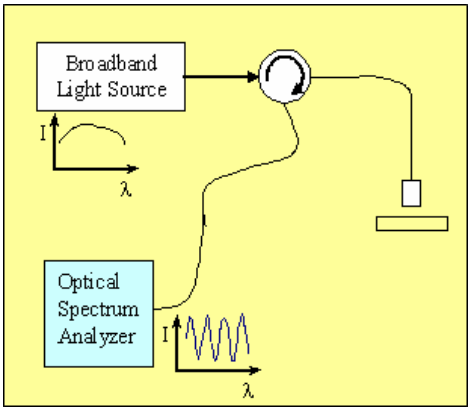

Figure 2.2 LPFG based WLI distance sensor

solid arrow. At the end of the optical fiber, the light beam exits the probe, propagates in the air, then is reflected by the sample, and finally is coupled back to the fiber core and propagates toward the LPFG. The light that is coupled into the cladding by the LPFG propagates along the

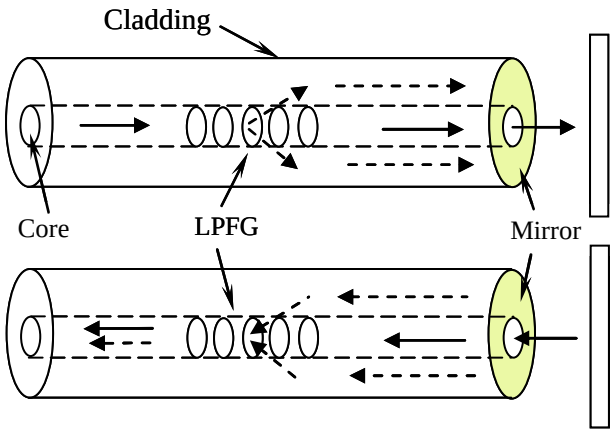

Figure 2.3 Cladding coated sensor probe

cladding (dashed arrows in Figure 2.3), until it reaches the mirrored end of the probe. This cladding mode will trace its path back to the LPFG after reflecting from the mirror. Based on the reciprocity principle of light propagation, the reflected cladding mode will be coupled back to the core mode. When the cladding mode is recombined with the core mode, the two light waves interfere constructively and destructively because of the different optical paths they have traveled. By routing these two reflected lights to the OSA using the optical circulator, the interference fringe spectrum can be measured.

The OPD between the core mode and the cladding mode is obtained by the difference between the refractive indices of the cladding and the fiber core, and the cavity between the fiber end and the sample surface, *i.e.*,

$$OPD = 2\left(\Delta nL + n_m d\right) \tag{2.1}$$

where $\Delta n = n_{clad} - n_{core}$ is the difference between the refractive indices of the fiber core and cladding, L is the distance between the LPFG and the fiber end, n_m is the refractive index of the medium in the free space (for air, $n_m=1$), and d is the cavity distance between the fiber end and

the sample. Without the presence of the LPFG and the mirrored fiber end, figure 2.3 is reduced to the FPI distance sensor where the two interfering light waves are formed by the light reflected from the fiber/air interface and that reflected from the sample surface. Therefore, the LPFG-based distance sensor is similar to the FPI distance sensor except that its OPD is contributed by both the LPFG cavity distance *L* and the FPI cavity distance, which is equal to the target distance *d*.

For a whitelight interferometric sensor, from Chapter 1, the general expression for the fringe spectrum as a function of the wavelength λ is

$$R(\lambda) = R_1 + R_2 + 2\sqrt{R_1 R_2}\cos(2\pi OPD/\lambda + \theta), \quad (2.2)$$

where R_1 and R_2 are the intensities of the two interfering beams and θ is the phase shift. For a whitelight FPI distance sensor, $OPD=2n_m d$. Therefore, Eq. (3) becomes

$$R(\lambda) = R_1 + R_2 + 2\sqrt{R_1 R_2}\cos(4\pi n_m d/\lambda + \theta). \quad (2.3)$$

As discussed earlier in Chapter 1, the measurement of distance requires the presence of at least two fringes within the bandwidth of the whitelight source. This imposes a limit on the smallest distance a FPI distance sensor can measure. For a LPFG-based distance sensor, however, the reflectance $R(\lambda)$ depends on both ΔnL and *d*, whereby

$$R(\lambda) = R_1 + R_2 + 2\sqrt{R_1 R_2}\cos[4\pi(\Delta nL + d)/\lambda + \theta]. \quad (2.4)$$

Therefore, the distance *d* can be arbitrarily small as long as the additional OPD term ΔnL is large enough so that a minimum number of fringes are presented.

2.2.2. Sensor Fabrication

The LPFG-based distance sensor requires the integration of two optical fiber concepts; a mirrored surface that only covers the cladding region of the optical fiber and an LPFG that couples a part of the incoming light into the cladding region.

2.2.2.1. Fabrication of cladding coated sensor probe

The concept of the fabrication process is illustrated in Figure 2.4. First a negative photoresist is deposited on the fiber end. Ultraviolet light is then coupled into the end of the optical fiber that is not coated with the photoresist (Figure 2.4 a). Because of the multimode propagation of the UV light in the SMF, the UV light is confined within the fiber core and thus only cures the photoresist covering the fiber core when it exits the optical fiber at the other end. As a result, the fiber core is masked by the cured photoresist while the uncured photoresist is removed (Figure 2.4 b). Metallic thin film is then deposited on the cladding region and the photomask (Figure 2.4 c). Finally, the photomask is etched to expose the fiber core again (Figure 2.4 d).

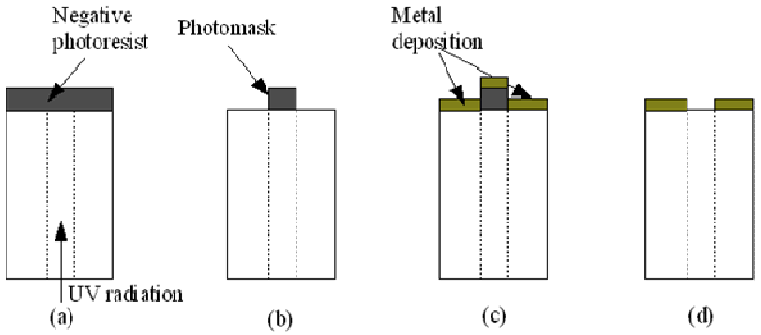

Figure 2.4 a) Deposition of photoresist on the fiber. b) Photomask after the photoresist is cured with UV light and the uncured photoresist is washed away. c) After metal deposition. d) After the photomask is dissolved in alcohol.

The experimental setup for coupling the UV light to the optical fiber is shown in Figure 2.5. A UV light-emitting diode (LED) (Nichia NSHU550A, wavelength 375 nm, see Appendix D) was chosen as the UV light source. The cleaved optical fiber was mounted on a three-axis fiber alignment stage and manually aligned with the LED. Different coupling mechanisms were experimented. It was discovered that the maximum coupling from the LED to the optical fiber is achieved by removing the glass cover of the LED and directly butting the optical fiber against the LED chip. An optical power meter was employed to monitor the output power of the optical fiber during the alignment process in order to provide position feedback for the alignment. With

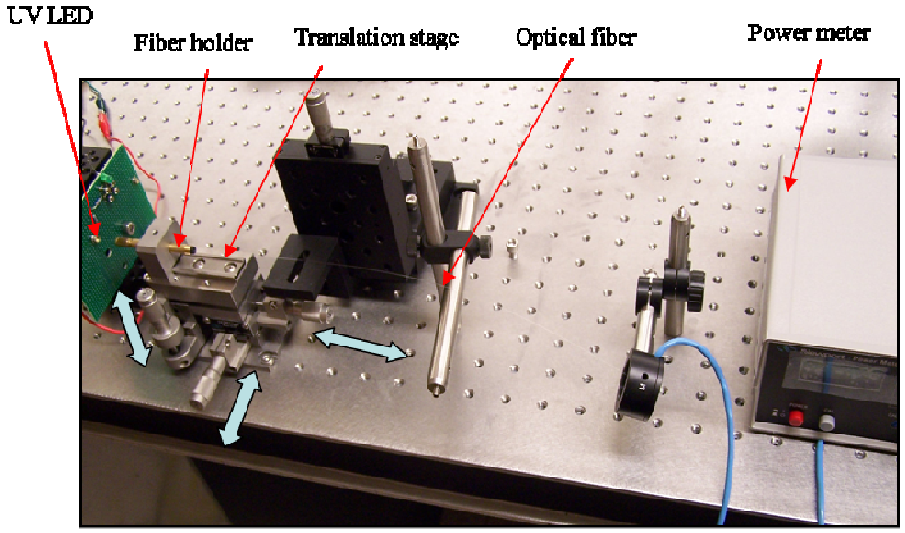

Figure 2.5 Experimental set up to fabrication the sensor probe

a forward current of 50 mA supplied to the UV LED, an output power of 180 nW was achieved at the end of a 50 cm long SMF. Even though the total output power was low, the power density of the UV light was sufficient to cure the epoxy in a short time. The intensity of the UV light can be conveniently adjusted by changing the supplied current. It is worth noting that the optical fiber should be long enough so that the UV light coupled into the fiber cladding is attenuated and only the light propagating in the fiber core remains.

After one end of the SMF was aligned with the LED chip, the free end of the SMF was dipped into a pool of UV-curable optical adhesive (Norland Products, NOA61, see Appendix C) and quickly removed from it. Due to the surface tension, a small amount of uncured epoxy was deposited, forming a dome at the end of the optical fiber. The UV LED was then switched on, exposing the uncured epoxy with the UV light. After irradiating the NOA61 for one to two minutes, a polymer tip was formed on the top of the fiber core, as shown in Figure 2.6 a. After the epoxy was fully cured, the fiber end was washed in acetone in order to remove any uncured epoxy from the surface. Inspecting the fiber end surface using an optical microscope revealed that a clean surface was obtained, as shown in Figure 2.6 b. Metal deposition was then carried out in a sputtering machine (CrC-100) at 100 mA for 3 minutes. After metal deposition, the

surface was inspected again under the microscope to make sure that a good quality metallic

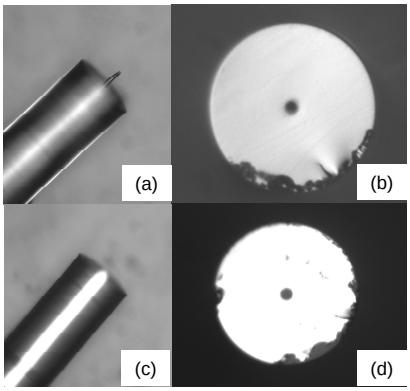

Figure 2.6 Micrographic images of the sensor probe at different fabrication steps

coating was achieved. The final fabrication step involves submerging the fiber end in Acetone for 40-50 seconds to dissolve the cured polymer tip. Micrographic images of the SMF afterwards confirm that the polymer tip has been removed and the fiber core is exposed again, as shown in Figures 2.6 c and 2.6 d.

2.2.2.2. Mechanically Induced LPFG

An LPFG can be either permanently engraved in a SMF using a high power UV laser or mechanically induced by introducing periodic micro-bending as shown in Section 2.1. Mechanically induced LPFG is preferred for our purpose because the LPFG cavity distance can

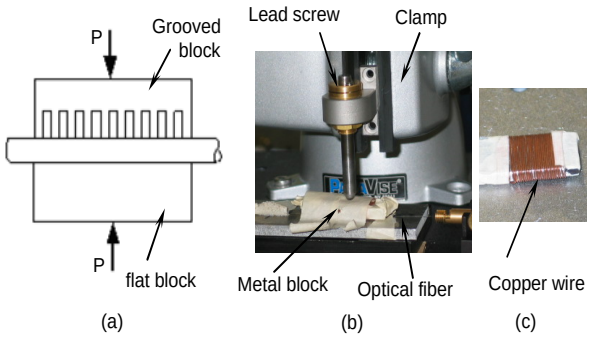

Figure 2.7 Mechanically-induced LPFG

be easily adjusted. A diagram of a mechanical induced LPFG is shown in Figure 2.7 a. A conventional SMF is placed between two metal blocks; one with periodic notches and one with

a flat surface. As pressure is applied to the metal blocks, micro-bending is introduced into the fiber, generating LPFG mode-coupling effect. The properties of the LPFG are determined by the length of the metal blocks, the period of the notches, and the pressure applied. The implementation of the mechanically induced LPFG is shown in Figure 2.7 b. Instead of using a

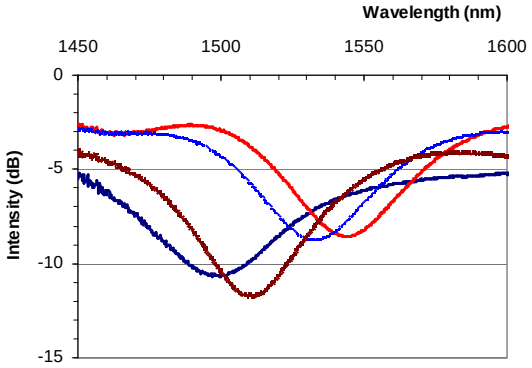

Figure 2.8 Difference spectra obtained using mechanically induced LPFG

grooved block, an aluminum block wound with a copper wire of 500 μm in diameter was employed to apply periodic pressure to the optical fiber (see Figure 2.7 c). A 100 turn-per-inch (TPI) lead screw was clamped on top of the metal block so that the applied pressure can be easily controlled by adjusting the lead screw. As shown in Figure 2.8, the set-up was flexible in order to achieve the resonance loss of the LPFG at different frequencies.

2.2.3. Experimental Setup

The performance of the LPFG-based WLI distance sensor was evaluated using the experimental setup shown in Figure 2.9. The mechanically-induced LPFG described in section 2.2.2.2 was mounted on an elevated platform. The cladding-coated optical fiber probe was held in front of a mirror with the help of a fiber chuck clamped in a V-groove holder. A mirror, serving as the target, was placed on a rotation stage in order to help align the mirror parallel to the optical fiber end. This, in turn, was mounted on top of a horizontal translation stage. The movement of the translation stage was controlled by a motorized actuator. A servo controller

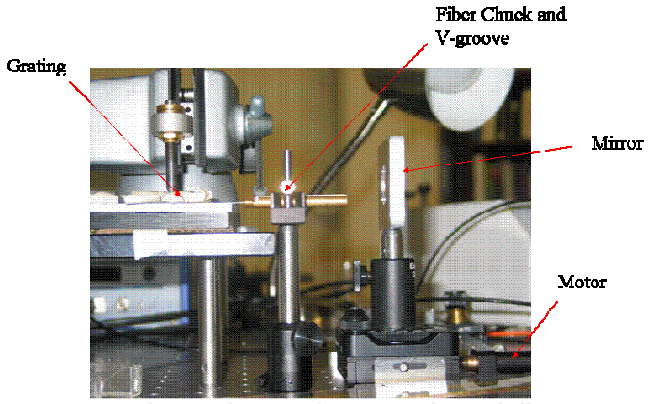

Figure 2.9 Experimental setup for LPFG-based distance sensor

(Thorlabs APT-DC) was employed to control the motor and to provide feedback on the mirror position. An Erbium Doped Fiber Amplifier (EDFA) with a wavelength bandwidth of 40 nm (1540~1580 nm) was utilized as the broadband light source. The transmission spectrum of the mechanically induced LPFG was adjusted accordingly to fall within this range.

2.2.4. Results

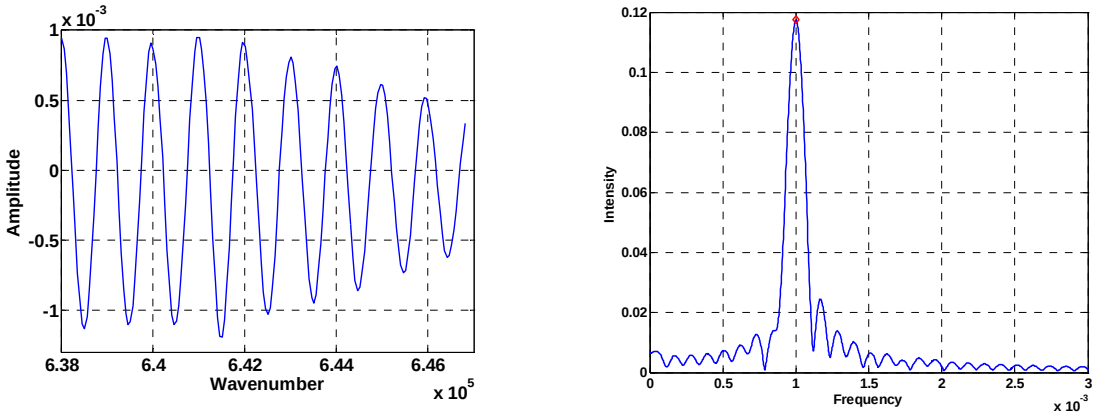

Figure 2.10 The reflectance spectrum and its FFT without the presence of mirror

The fringe spectra of the LPFG-based distance sensor, acquired at different cavity distances, were first normalized with the spectrum of the laser source. After converting the data from the wavelength scale to the wavenumber scale, Fast Fourier Transform (FFT) was applied to the fringe spectra in order to obtain their frequency components (see Appendix A). From

chapter 1, we know that the frequency position f_p of the FFT peak is directly correlated to the OPD, i.e. f_p=*OPD*. Therefore, for a LPFG-based WLI distance sensor, the free-space cavity distance *d* can be calculated from the FFT peak frequency directly if ΔnL is known, assuming n_m=1. During the course of the experiment, it was noted that interference fringes could still be observed even when the mirror was not placed in front of the sensor probe. These fringes are due to the interference between the reflected light in the cladding mode and the core mode reflected at the fiber/air interface, *i.e*. the Fresnel reflection. Because the frequency of this fringe spectrum is determined by the LPFG product ΔnL only, this proves to be of advantage since it enables the precise determination of ΔnL. Based on the FFT spectrum shown in Figure 2.10, the ΔnL product for our sensor was calculated to be around 503.14 μm. Since the cavity

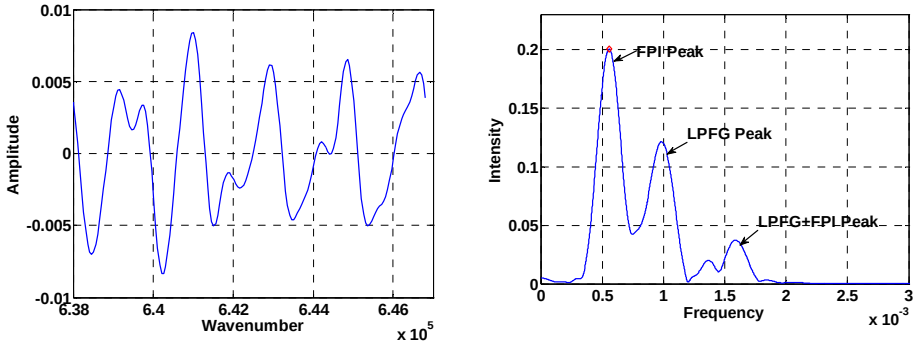

Figure 2.11 (a) & (b) Fringes from three interferences and its FFT.

distance *L*, measured roughly from the center of the grating to the fiber end, was 11.5 cm, the refractive index difference Δn between the fiber cladding and the fiber core is estimated to be 0.0043, which is close to the typical Δn value of 0.003 for a SMF.

When a mirror is placed in front of the sensor probe, the reflectance spectra are due to the following three interferences:

I. The interference between the reflected cladding mode and the core mode reflected by the fiber/air interface, *i.e.,* the LPFG effect.

II. The interference between the core mode reflected at the fiber/air interface and the core more reflected by the mirror, *i.e.*, the FPI effect.

III. The interference between the reflected cladding mode and the core mode reflected by the mirror, *i.e.,* the combined LPFG and FPI effect (LPFG + FPI interference).

The LPFG fringe spectrum, *i.e.,* from interference I, is independent of the FPI cavity distance *d* and is identical to the fringe spectrum obtained when the mirror is not presented. The other two interferences, however, are directly controlled by the cavity distance *d*. The resulting interference fringes from these three interferences are shown in Figure 2.11 a. The FFT of the interference fringes clearly demonstrated the existence of the three interferences, as shown in Figure 2.11 b. The locations of the three frequency peaks in the FFT spectrum correspond to the OPD of the three interferences.

Based on Equation (1), the OPD of the LPFG+FPI interference is equal to the OPD of the LPFG interference plus that of the FPI interference. Therefore, the frequency spacing between the FPI peak and the LPFG+FPI peak in the FFT spectrum should be equal to the frequency of the LPFG peak, a constant value determined by ΔnL. At a large cavity distance *d*, the FPI frequency peak can be easily identified from the FFT of the reflectance spectrum while

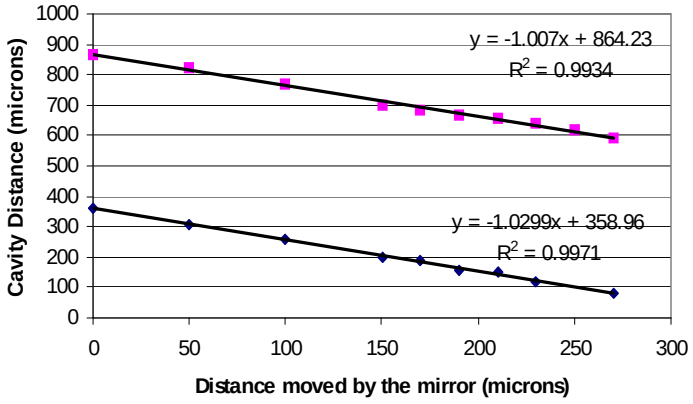

Figure 2.12 Distances estimated from the FPI and the LPFG+FPI interference fringes.

the LPFG+FPI interference has a low visibility (see Figure 2.13 b). Since the frequency location of the LPFG+FPI interference can be calculated from the frequency locations of the LPFG and FPI interferences, an appropriate bandpass filter can be designed to isolate the fringes contributed by the LPFG+FPI interference and thus improve its visibility.

Figure 2.12 compares the cavity distances measured from the FPI interference and those measured from the LPFG+FPI interference. The distance between the sensor probe and the mirror was adjusted by traversing the mirror using the motorized translation stage. The mirror was moved towards the sensor in steps of 20 μm. Since absolute distance is measured, therefore a slope of 1 is expected when the distance measured by the FPI and LPFG+FPI peaks are plotted against the distance moved by the mirror. As shown in Figure 2.12, a slope of 1.007 and 1.0299 is obtained over the entire range of measurement by LPFG+FPI and the FPI peaks respectively.

At each position, the reflectance spectrum of the LPFG-based WLI distance sensor was recorded, from which the cavity distance was calculated from the positions of the FPI peak and the LPFG+FPI peak independently. As shown in Figure 2.12, the distances measured from

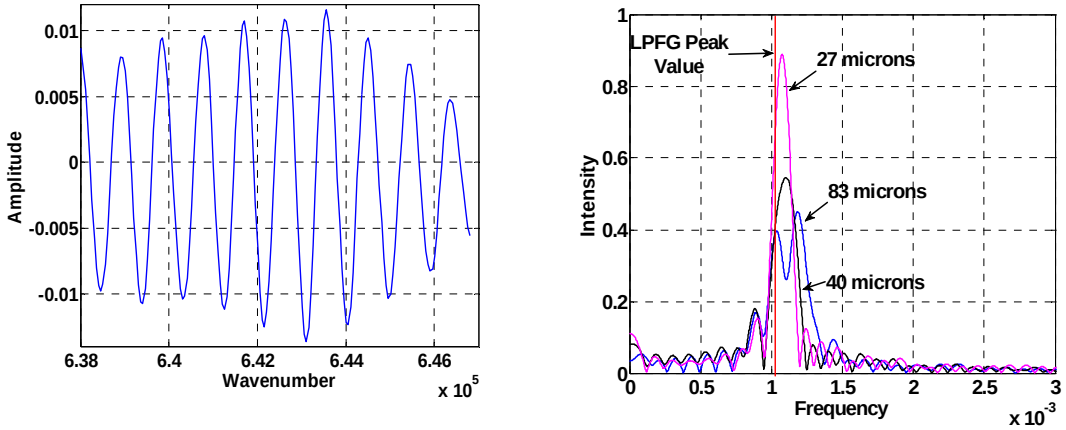

(a) (b)

Figure 2.13 a) Filtered reflectance spectrum at a distance smaller than 83 μm; b) FFTs of the reflectance spectra at small distances.

both interferences demonstrated a linear relationship with the traversed distances, calculated from the motor position feedback. In addition, the two lines are parallel to each other, indicating that the difference between the FPI cavity distance and the LPFG+FPI cavity distance always remains a constant and is equal to the ΔnL product obtained earlier. As the free-space cavity distance *d* reduces, the FPI peak will shift toward a lower frequency while the LPFG+FPI peak will shifts toward the stationary LPFG peak. In other words, the number of fringes presented in a given spectral bandwidth reduces. When the cavity distance *d* is less than 83 μm, the number of fringes generated by the FPI effect is too small for the FPI peak to be visible in the FFT spectrum. Due to the contribution of the LPFG cavity, the LPFG+FPI peak would still be visible. Therefore, the free-space cavity distance *d* can still be measured from the LPFG+FPI peak even though it is too small to be measured from the FPI interference. Figure 2.13 (a) shows the filtered reflectance spectrum of the LPFG-based WLI distance sensor at a distance that the FPI fringes are no longer presented. The shift of the LPFG+FPI frequency peak in the FFT spectrum, as the cavity distance *d* decreases, is shown in Figure 2.13 (b). At 83 μm, two distinct frequency peaks, *i.e.* the LPFG peak and the LPFG+FPI peak, can be resolved clearly and they have roughly the same intensity. As the distance reduces to 40 μm, the LPFG+FPI peak starts to merge with the LPFG peak. Since the intensity of the LPFG+FPI peak has increased beyond the intensity of the LPFG peak, the frequency location of the LPFG+FPI peak can be easily

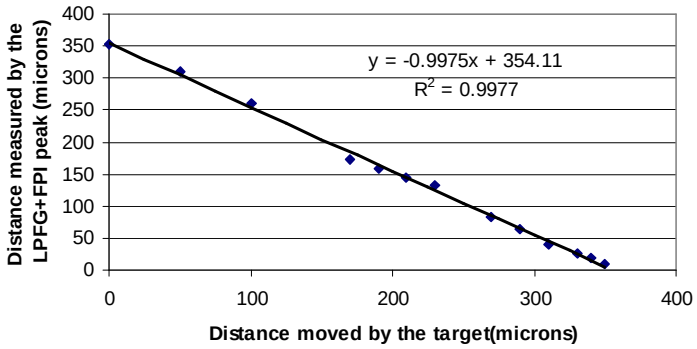

Figure 2.14 Linear relationship between the distances moved by the target and the distances measured by the LPFG-based WLI distance sensor.

identified from the FFT spectrum. As the distance reduces even further to 27 μm, only the LPFG+FPI peak remained, from which the cavity distance *d* can still be calculated. Figure 2.14 shows the relationship between the distance traversed by the translation stage as well as the distance measured from the LPFG+FPI peak. Since in this case also absolute distance was measured, a slope of 1 is expected over the entire measurement range. A linear relationship is demonstrated over the cavity distances ranging from 350 μm to 4 μm with a slope of 0.9975.

2.2.5. Conclusions

In this chapter the development of an LPFG based distance sensor was discussed. The performance of the distance sensor was evaluated and it was observed that it could measure a distance down to 4 μm successfully, which is significantly lesser than the EFPI distance sensor.

Although the sensor satisfies all the objectives that were defined in Section 1.2, the bulky nature of the mechanically induced LPFG makes it difficult to install and therefore limits its applications. Furthermore, the coat of optical fiber between the LPFG and the mirrored end has to be stripped off to reduce the optical loss of the cladding mode. This long section of bare fiber make the LPFG based sensor very fragile. As a result, a more flexible and robust sensor configuration is called for.

CHAPTER 3

ARBITRARY SMALL DISTANCE MEASUREMENT WITH A POLYMER TIP

The LPFG based WLI distance sensor can measure arbitrary small distances because of the additional OPD contributed by the cavity between the LPFG and the fiber end. The same effect can be achieved by fabricating a polymer tip at the end of an optical fiber. If the refractive index of the polymer tip is different from that of the optical fiber core, this introduces an additional interference cavity. Therefore, the polymer tip serves the same function as the LPFG. This chapter discusses the development of such a polymer tip based small distance sensor. Its fabrication, setup, and performance are described in detail.

3.1. Principle of Operation

A diagram of the optical fiber polymer tip based distance sensor is given in Figure 3.1. A polymer core is fabricated at the end of an optical fiber. A part of the light traveling in the fiber core is first reflected at the fiber /polymer interface. The transmitted light then travels inside the polymer core and again is partially reflected at the polymer core/air interface. The rest of the light exits the polymer tip, travels in the medium and finally gets reflected by the mirror. When these three reflected light are recombined in the optical fiber, they interfere with each other due to the different optical paths they have traveled. For the light reflected at the fiber/polymer interface I_1 and the light reflected at the polymer/air interface I_2, their interference spectrum can

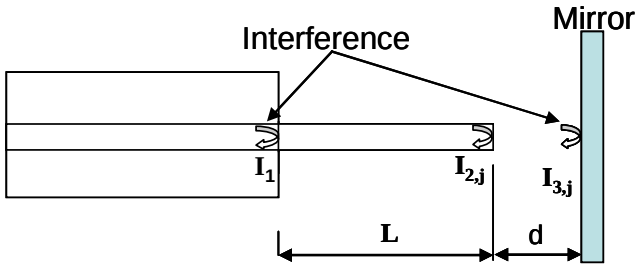

Figure 3.1 Optical Fiber with polymer tip

be expressed as

$$I = I_1 + I_2 + 2\sqrt{I_1 I_2}\cos(\phi). \tag{3.1}$$

The phase shift ϕ is related to the OPD between these two lights. Because the polymer core does not have a cladding region, it operates as a multi-mode fiber (n_{core} = 1.56, n_{clad} = 1.0, V =23 at 1310 nm) guiding higher order modes inside the polymer core.

Therefore, the FP interference due to both the fundamental mode and the higher order modes i.e.[13],

$$I(\lambda) = \sum_j \left[I_1 + I_{2,j} + 2\sqrt{I_1 I_{2,j}}\cos(\phi_{12,j}) \right], \tag{3.2}$$

where $I_{12,j}$ is the intensity of the light converted from the j^{th} mode to the fundamental mode. The phase shift between I_1 and $I_{12,j}$ i.e., $\phi_{1,2j}$ is governed by the length and the effective refractive index of the polymer tip.

The interference between the light reflected by the mirror $I_{3,j}$ and the fiber/polymer reflection I_1 can therefore be written as

$$I(\lambda) = \sum_j \left[I_1 + I_{3,j} + 2\sqrt{I_1 I_{3,j}}\cos(\phi_{13,j}) \right], \tag{3.3}$$

where $\phi_{1,3j}$ represents the phase shift between I_1 and $I_{3,j}$ and is given by

$$\phi_{13,j} = 2\left(\phi_{12,j} + \frac{2\pi n_m d}{\lambda} \right), \tag{3.4}$$

where d is the distance to be measured between the polymer tip and the mirror. When d is large, it can be only measured from the fringe spectra due to the interference of $I_{2,j}$ and $I_{3,j}$. When d is very small, however, it can only be measured for the interference spectrum due to

the interference of $I_{1,j}$ and $I_{3,j}$. Since the quantity $\phi_{12,j}$ in equation (9) depends on the properties of the polymer core, the distance *d* can be calculated from the phase shift $\phi_{13,j}$ as long as the phase shift $\phi_{12,j}$ is known. This is similar to the principle of operation of the LPFG-based arbitrary small distance sensor. As discussed in Section 2.2.1, the LPFG-based distance sensor is capable of measuring small distances due to the additional OPD, contributed by the LPFG cavity. Similarly, the same effect can be obtained using the polymer-tip based distance sensor because the polymer tip also introduces an additional OPD to a conventional EFPI distance sensor.

3.2. Sensor Fabrication

The fabrication technique described in Section 2.2.2.1 was extended to fabricate the polymer tip at the end of the fiber. In order to control the length of the polymer tip, two SMFs facing each other were first aligned under a microscope using the setup shown in Figure 3.2. The alignment mechanism consists of two V-grooved fiber holders. One is stationary while the other is mounted on a three-axis translation stage. The fiber on which the polymer tip is to be fabricated is mounted on the stationary stage. The other fiber is aligned to face the original fiber using the three-axis stage. An optical microscope on top allows us to view the alignment at a greater magnification and therefore perform finer adjustments.

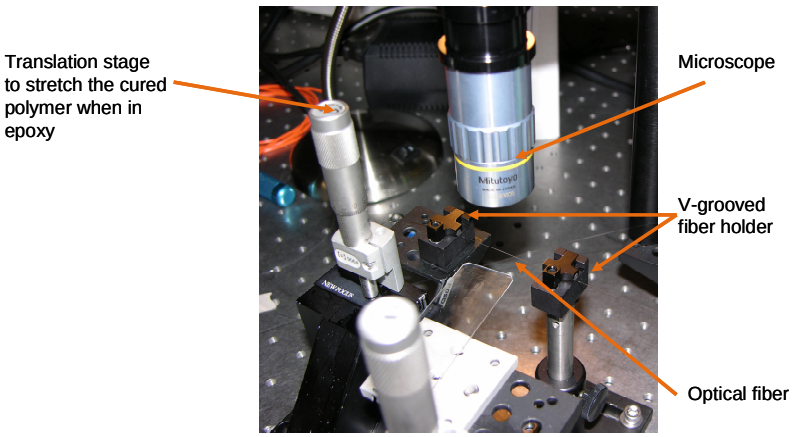

Figure 3.2 Experimental setup for fiber alignment

The gap between the two fibers can be changed by using the three axis translational stage, therefore allowing us control over the polymer core length.

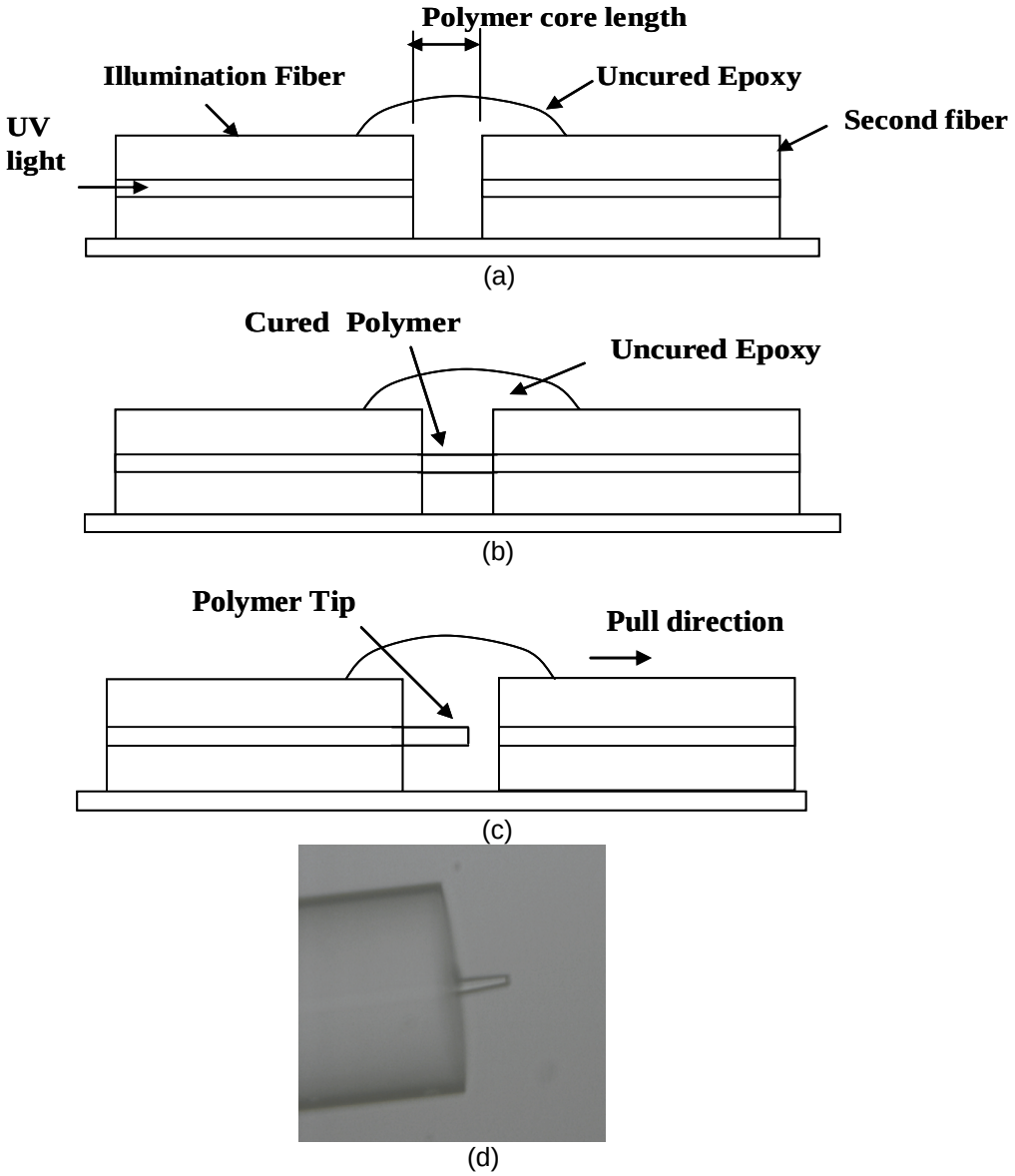

Figure 3.3 a) Two SMFs facing each other in uncured epoxy with the desired polymer length gap between them. b) Polymer formed between the two fibers are curing from one end. c) One of the fibers is pulled and the polymer tip is formed on the fiber from which the UV light was passed. d) Image of a polymer tip 36 µm in length and 8 µm in diameter.

After the two fibers were aligned, they were subsequently submerged into the UV curable epoxy, as shown in Figure 3.3 a. UV light was coupled into the free end of the illumination fiber. When the UV light exited the illumination fiber, it cured a polymer core between the two fibers (see Figure 3.3 b). Once the polymer core was formed, one of the fibers was slowly pulled away from the other using the translation stage, as shown in Figure 3.3 c. Because the polymer core has a stronger bond to the illumination fiber than the second fiber, it breaks off from the second fiber first and remains attached to the illumination fiber. Further, the polymer core returned to its original shape after the separation, due to its elastic properties. A micrographic image of the fabricated polymer core in alcohol is shown in Figure 3.3 d.

3.3. Experimental Setup and Results

The experimental setup and procedure for evaluating the polymer tip based sensor is identical as that used for the LPFG-based sensor (see Figure 2.3). The quantity $\phi_{12,j}$ was calculated from the frequency of the interference spectrum when the mirror was not present in front of the polymer tip. Based on the FFT spectrum shown in Figure 3.4, length of the polymer

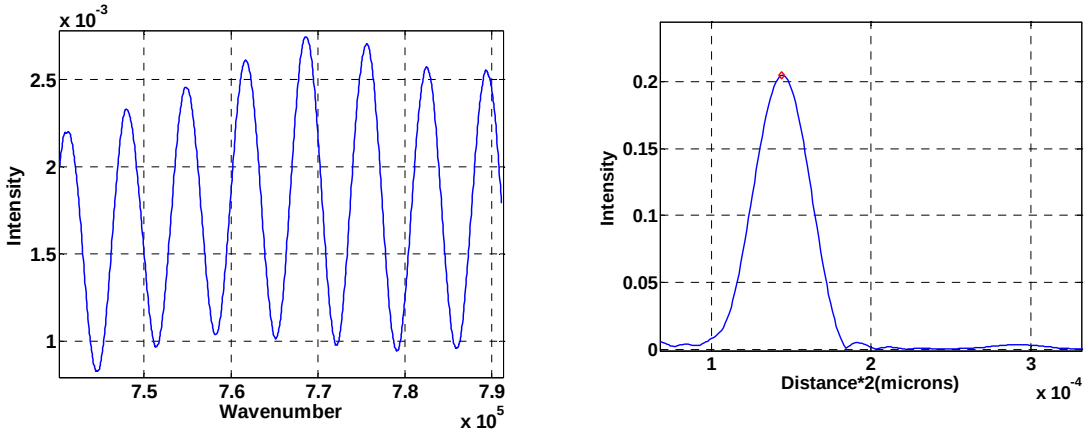

Figure 3.4 Filtered signal and its FFT spectrum without the presence of the mirror

core was found to be 37μm from which $\phi_{12,j}$ can be calculated.

Similar to the LPFG-based sensor, the reflectance spectra of the polymer tip sensor in the presence of the mirror is due to the following three interferences:

I. Interference between the light reflected at the end of the polymer core and the light at the fiber/polymer interface (see Figure 3.5 a).

II. Interference between the light reflected at the mirror and the light reflected at the end of the polymer core (see Figure 3.5 b).

III. Interference between the light reflected at the mirror and the light reflected at the fiber/polymer interface (see Figure 3.5c).

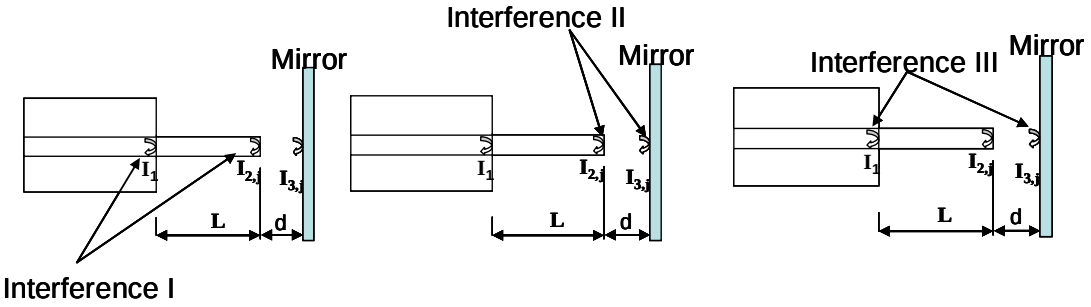

Figure 3.5 Schematic representation of a) Interference I b) Interference II c) Interference III

The three interferences show up as three different frequencies in the FFT as shown in Figure 3.6. The frequency peak of interference I is independent of the distance between the polymer tip and the mirror. As a result, it remains at the same location as the distance changes. Interference II is the same as the F-P interference. Therefore the frequency peak of this interference will shift toward a lower frequency as the cavity distance *d* reduces. In other words, the number of fringes obtained in the spectrum starts reducing. Because the bandwidth of the broadband source we used for the polymer tip based distance sensor was larger than the bandwidth of the source we used for the LPFG based distance sensor, the polymer tip based

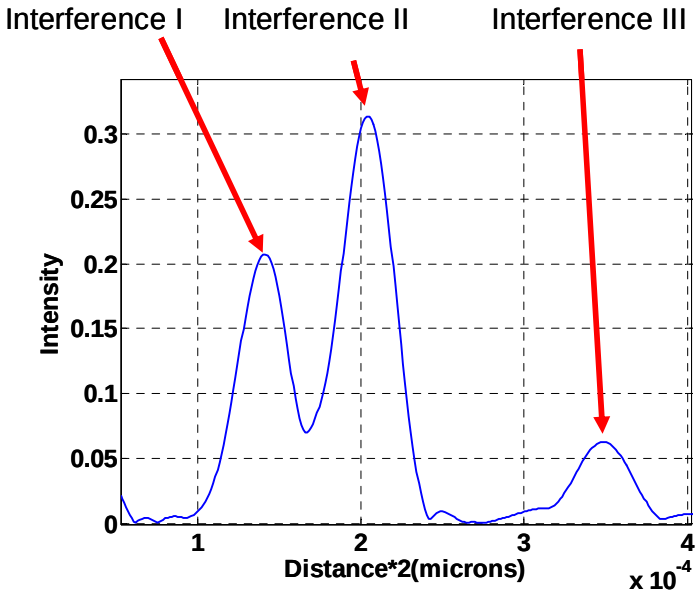

Figure 3.6 FFT showing three interferences

distance sensor was able to measure a smaller distance from interference II, compared to the LPFG based distance sensor. However at distances less than 23 μm, the peak due to interference II is no longer visible in the FFT spectrum since the number of fringes is too small. Due to the contribution of the polymer core to the OPD of interference III, its frequency peak is still visible and therefore can still be used to measure distance.

Figure 3.7 shows the FFT of the filtered spectrum when the peak due to interference II is no longer presented. At *d* = 23 μm, the FFT shows two peaks with roughly the same intensity.

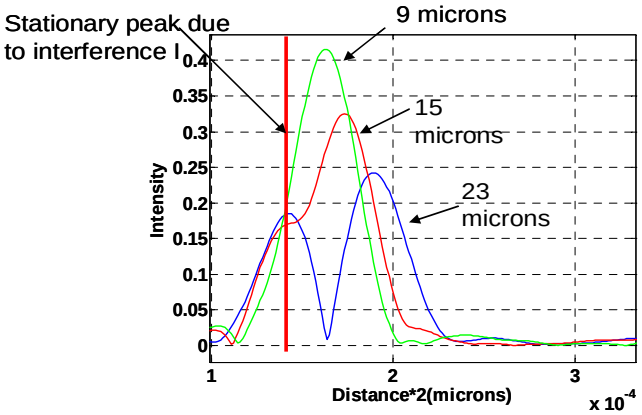

Figure 3.7 FFT of the filtered spectrum at distances less than 23 μm.

The lower frequency peak is due to interference I and the higher frequency peak is due to interference III. As the distance reduces to 15μm, the peak due to interference III starts to merge into the peak due to interference I. Since the intensity of the peak due to interference III

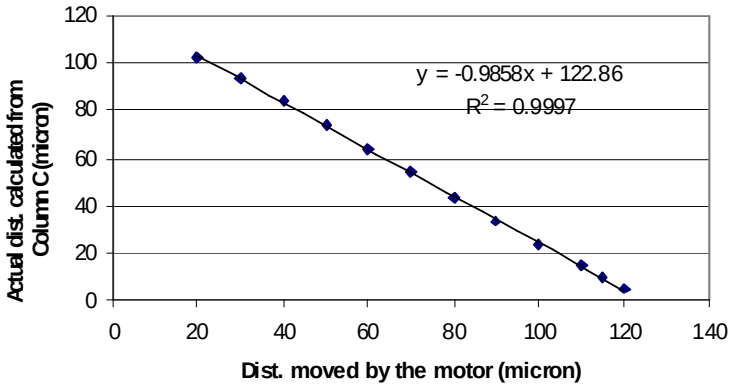

Figure 3.8 Linear relationship between the distances moved by the target and the distances measured by the polymer tip based distance sensor.

has increased beyond that of interference I, its location can be easily identified. As the distance reduces even further only the peak due to interference III is present, from which the cavity distance *d* can still be calculated. Figure 3.8 shows the relationship between the distance traversed by the translation stage and the distance measured from the peak due to interference III. Since absolute distance from the mirror was measured, a slope of 1 is expected over the entire distance range. As shown a linear relationship with a slope of 0.9858 is demonstrated. The smallest distance we measured using the polymer tip based distance sensor was 4 μm. This is much smaller than what the EFPI technique can measure, which is 23 μm.

3.4. Conclusions

This chapter described the principle of operation, the fabrication, and the evaluation of a polymer tip based optical fiber sensor for small distance measurement. It was demonstrated that the polymer tip based distance sensor is capable of measuring distances as small as 4 μm. Compared to the LPFG based WLI distance sensor, the polymer tip based distance sensor is easier to implement and is much more compact. Furthermore, the polymer core fabrication

technique can be extended to fabricate sensor probes that can measure other quantities such as refractive index and strain.

CHAPTER 4

REFRACTIVE INDEX MEASUREMENT

Various chemical substances as well as several different physical and biological parameters can be detected through the measurement of refractive index (RI). This has motivated the optical fiber sensor community to put a lot of effort in developing optical fiber RI sensors. Optical fiber RI sensors have found applications in in-situ monitoring of chemical processes in harsh environments, as well as pollution monitoring in water supply and other public utilities. Many different RI principles such as interferometry, fiber gratings, and specialty fibers [14-20] have been proposed to design optical fiber RI sensors.

Interferometer-based RI sensors consist of two beams; one beam is exposed to the external medium and thus serves as the sensing arm while the other beam is used as the reference. When these two arms are combined to generate an interference pattern, a change in the external RI alters the optical path length of the sensing arm and thus causes a shift in the interference pattern. These types of sensors often require a mechanism to split the incoming light into two arms, resulting in a complicated sensor system.

Two types of fiber gratings, viz., Fiber Bragg Grating (FBG) and Long Period Fiber Grating (LPFG), are commonly exploited for RI measurement. RI changes are measured from the shifts of the transmission/reflectance spectra due to the influence of the external RI on the coupling conditions of the fiber gratings. Because an LPFG couples the light from the core mode to the cladding modes, its transmission spectrum is highly sensitive to changes of the external RI [15]. By comparison, the FBG-based RI sensors are usually much less sensitive. Therefore, the cladding surrounding a FBG is often etched or thinned in order to increase the sensitivity [16,17]. RI sensors based on fiber gratings are usually expensive because of the stringent grating fabrication processes. Specialty fibers such as D-shaped fiber [18],

microstructured fiber [19], and cladding stripped fiber [20] have also been used for biochemical sensing. These types of optical fiber biochemical sensors require accessing the evanescent field at the interface of the fiber core and the surrounding medium. As such, precision micromachining is required in order to remove a part of the fiber cladding.

This chapter describes the development of an optical fiber RI sensor based on the polymer tip fabricated at the end of the optical fiber. A simulation model was developed to understand the sensing mechanism. The performances of the sensor were evaluated using five different refractive index standards.

4.1. Principle of Operation

The sensor probe used for distance measurement in Chapter 3 can also be used to measure refractive index. Such a sensor offers a low cost alternative to present RI sensor technologies with enhanced flexibility, robustness, and sensitivity.

The principle of operation of the polymer tip based RI sensor is quite similar to that of the distance sensor described in Chapter 3. The polymer core acts as a Fabry-Perot cavity, where the reflected fringe spectra is due to the interference between light reflected at the two ends of the polymer core as shown in Figure 4.1. Since the polymer core does not possess any cladding, it acts as a multimode fiber (n_{core} = 1.56, n_{clad} = 1.0, V =23 at 1310 nm), thus allowing higher-order modes to propagate inside the polymer core. Therefore, the F-P interference is a contribution of both the higher-order modes as well as the fundamental mode.

From equation (2) in Chapter 3, the interference pattern in the polymer core is given by

$$I(\lambda) = \sum_{j} \left[I_1 + I_{2,j} + 2\sqrt{I_1 I_{2,j}} \cos(\phi_j) \right], \qquad (4.1)$$

where ϕ_j represents the phase shift between I_1 and $I_{2,j}$ and $I_{2,j}$ is the intensity of the light converted from the j^{th} mode.

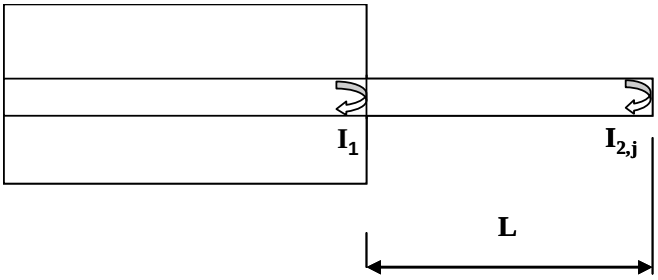

Figure 4.1 Diagram of the polymer tip

The quantity ϕ_j for the fundamental mode is given by

$$\phi_1 = 2\beta_1 L \ , \tag{4.2}$$

and for the higher-order modes it is given by

$$\phi_j = 2\left(\beta_1 L + \Delta\beta_{1j}\right)L, \tag{4.3}$$

where β_1 is the propagation constant of the fundamental mode and can be calculated from the wavelength λ, the refractive index of the polymer core n_1, the V number V, and the radius of the polymer core ρ by [21]

$$\beta_1 = \frac{2\pi n_1}{\lambda}\left[1-\left(\frac{U_{1\infty}e^{(-1/V)}\lambda}{2\pi\rho n_1}\right)^2\right]^{1/2} . \tag{4.4}$$

$U_{j\infty}$ is the modal parameter of the LP_{0j} mode. It is given by the root of the Bessel function of zero order, *i.e.,*

$$J_0(U_{j\infty}) = 0. \tag{4.5}$$

$\Delta\beta_{1j}$ is dependent on the properties of the polymer core and can be approximated as [22]

$$\Delta\beta_{1j} = \frac{(U_{j\infty}^2 - 2.404^2)\lambda}{4\pi\rho^2 n_1}\exp(-2/V) \tag{4.6}$$

The V number is dependent on the RI of the polymer core n_1 as well as that of the external medium n_{ext},[22] i.e.,

$$V = \frac{2\pi\rho\sqrt{n_1^2 - n_{ext}^2}}{\lambda}. \qquad (4.7)$$

Therefore a change in n_{ext}, will change the phase shift ϕ_j, causing a shift in the FP fringe positions. Comparing equation (3) with (6) indicates that the fringe shifts are mainly contributed by the phase shift of the higher-order modes.

4.2. Experimental Procedure

The polymer tip at the end of the optical fiber was fabricated using the same technique described in Section 3.2. A diagram of the experimental setup for refractive index measurement is shown in Figure 4.2. Once the polymer tip is formed and the uncured epoxy is cleaned off using alcohol, a small amount of the refractive index standard was dropped onto a glass slide.

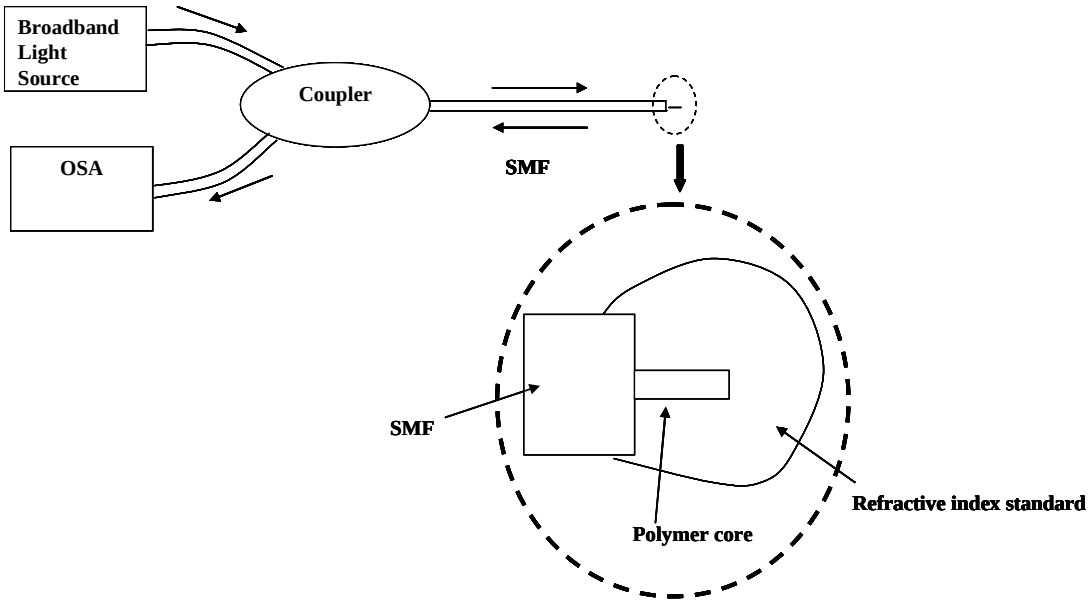

Figure 4.2 Experimental Setup for the RI sensor

The slide was then placed on a translation stage directly underneath the polymer tip. The slide was slowly traversed towards the polymer tip until the entire polymer tip was submerged in the refractive index standard. The interference spectrum was then observed on the OSA and measurements were made.

4.3. Results

A comparison of the fringe spectra of the sensor probe when it was immersed into two liquids with different refractive indices is shown in Figure 4.3. As the refractive index changes from 1.41 to 1.42, the fringes shifted towards the left. There is also a reduction in visibility of the fringe pattern since an increase in the external refractive index reduces the intensity of light reflected at the end of the polymer core.

A simulation model was implemented using Equations (4.1)-(4.7) in order to validate

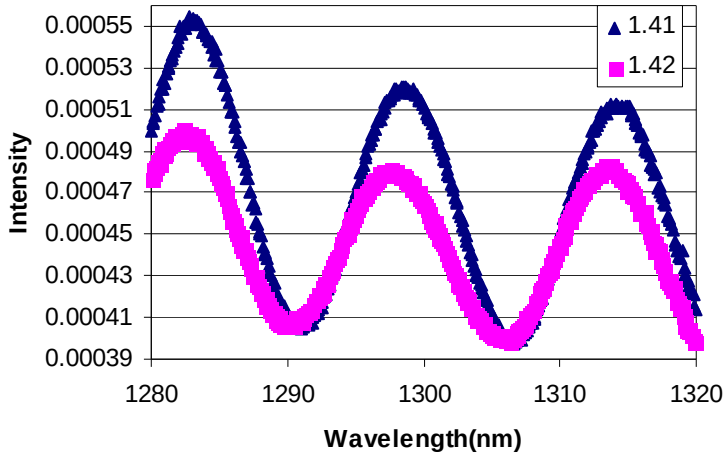

Figure 4.3 Reflectance spectra when the sensor is submerged in liquids with two different refractive indices

the experimental results. The length of the polymer core was determined by extracting the OPD from the reflectance spectra of the sensor when it was exposed to air. Five different refractive index standards (Cargille, #18065 series AA , 1.40-1.44) were used for measuring the response of the sensor. The fringe shifts obtained were fitted with a straight line and compared with that

obtained from the simulation (see Appendix B). The parameters used in the simulation were ρ = 4 µm, n_1 = 1.56, λ =1310 nm, and L= 36 µm. As shown in Figure 4.4, the experimental results

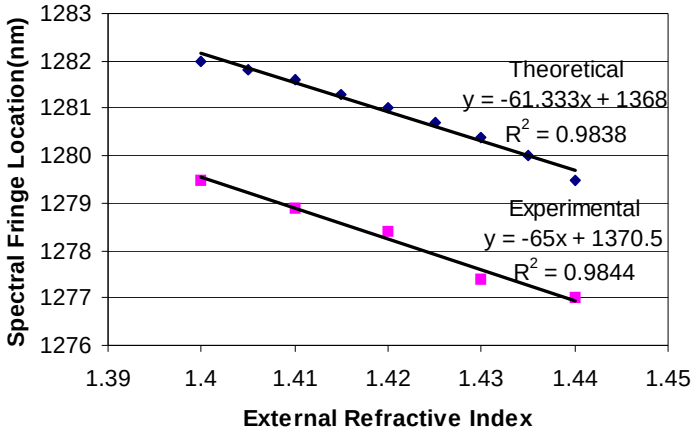

Figure 4.4 Comparison of sensor sensitivities obtained by theoretical analysis and experiment.

matched well with those obtained from simulation. A change of RI by 0.01 causes a shift of 0.6 nm in the fringe positions.

For comparison purposes, the fringe positions of the polymer core sensor were also calculated using the same wavelength as those reported by Ding *et.al.* [23] and Tian *et.al.* [24]. The simulation model predicted the polymer core sensor will shift the fringe by 0.47nm for a RI

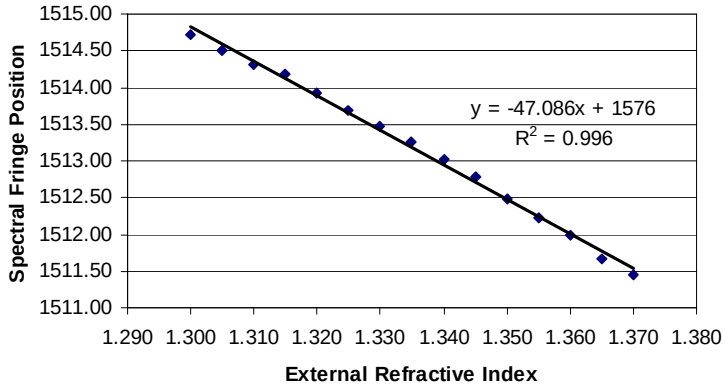

Figure 4.5 Sensitivity for the same wavelength range and RI measurement range as that of other LPFG and interferometric RI sensors

change of 0.01 over n_{ext} = 1.29~1.37, as shown in Figure 4.5. This sensitivity is about 60% higher than those obtained by LPFG [23] and interferometry [24] based RI sensors.

4.4. Conclusions

A compact and highly sensitive RI sensor was fabricated and its performance was evaluated using refractive index standards. The measurement results were verified analytically. The sensitivity of the sensor was found to be more than 60% higher than that obtained by other RI sensors. Moreover, the parameters of the polymer core sensor, such as the RI and the length of the polymer core, can be easily tailored to achieve the desired sensitivity and linearity range. The variations of these parameters and their impacts on the behavior of the sensor should be carried out in the future.

CHAPTER 5

STRAIN SENSOR

Optical fiber strain sensors have found great interest in the sensor community due to their compact size and ability to operate in a harsh environment. They can be easily multiplexed to monitor strain at multiple locations and are ideally suited for non destructive evaluation of components in spacecrafts, civil structures, and ships [25-27]. Their ability to monitor strain at multiple locations simultaneously presents a big advantage over present electronic strain gauges.

Ideally though, a strain sensor should have a lower stiffness and a higher fracture toughness than the host material. Most existing optical fiber sensors are silica-based optical fibers which usually have a large stiffness and can only sustain a maximum strains of about 3-5%. In general, silica-based optical fiber strain sensors are only reliable up to around 2% strain unless special preparation procedures are followed. Due to this mismatch of mechanical properties between the optical fiber and the host material, sensor fracture and debonding before the failure of the host structure are common.

To overcome this shortcoming, polymer optical fibers have been exploited for large strain measurement [28,29]. Polymer optical fibers though are restricted to 100m in length due to their high optical loss and multimode nature. Also polymer optical fibers mostly use an intensity-based measurement scheme which has poor accuracy as such a scheme is sensitive to environmental factors. The polymer used to fabricate distance and refractive index sensors earlier possesses low stiffness and therefore offers great potential for use as a strain sensor. In this chapter we describe the development of a strain sensor using this polymer and evaluate its performance.

5.1. Principle of Operation

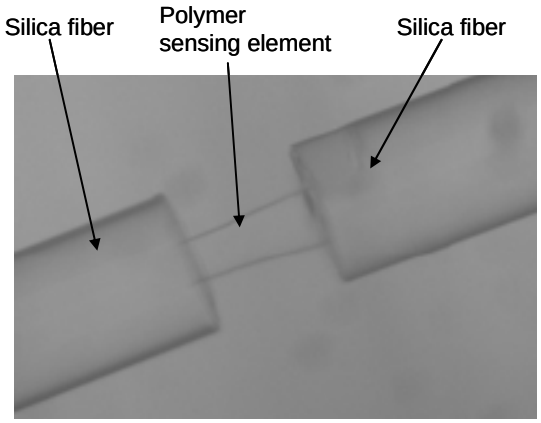

Figure 5.1 Micrograph image of the strain sensor.

A micrographic image of a hybrid silica/polymer optical fiber strain sensor is shown in Figure 5.1. The hybrid silica/polymer strain sensor is constructed by fabricating a tapered polymer fiber core between two silica optical fibers using UV irradiation. Broadband whitelight is transmitted from one optical fiber toward the other optical fiber through the polymer sensing element. Because there is a refractive index difference between the optical fibers and the polymer sensing element, a portion of the whitelight is reflected at the interface between the silica optical fiber and the polymer sensing element at both ends as shown in Figure 5.2.

For the light reflected at the fiber/polymer interface I_1 and the light reflected at the polymer/fiber interface I_2, their interference spectrum can be expressed as

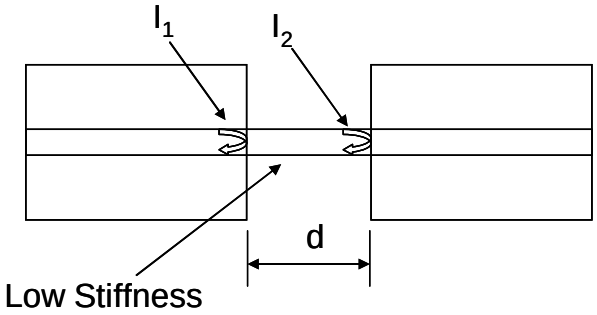

Figure 5.2 Diagram showing the principle of operation of the polymer based strain sensor.

$$I = I_1 + I_2 + 2\sqrt{I_1 I_2}\cos\left(\frac{4\pi nd}{\lambda} + \phi\right). \quad (5.1)$$

An applied strain alters the distance *d* between the two fibers therefore causing a shift in the frequency of the interference pattern. In return, the applied strain can be measured by monitoring the shift in frequency of the interference pattern.

The fabrication technique as described in Chapter 3 for manufacturing the polymer tip is also used to manufacture the polymer sensing element for the strain sensor, though in this case multimode fibers (MMFs) are used in place of SMFs and the polymer core remains attached to the second MMF as well. A micrograph image of the sensor fabrication process is shown in Figure 5.3. Figure 5.3 a shows the two MMFs aligned in the uncured epoxy before the UV LED is switched on. Figure 5.3 b shows the polymer core between the two fibers after it has been cured for 2~3 minutes.

5.2. Experimental Setup

The measurement system for strain is the same as that used for the distance and the RI measurements. It consists of a broadband source (BBS, Source of the Optical Spectrum

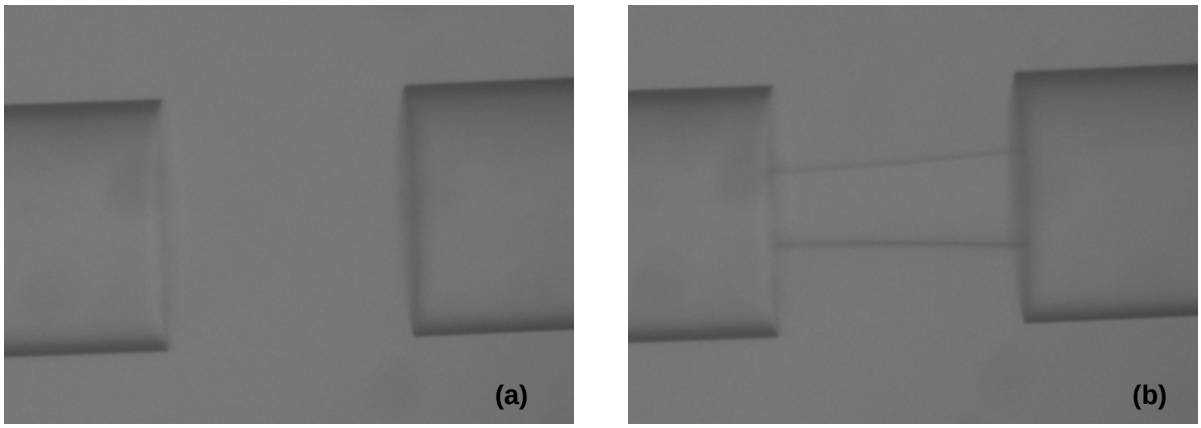

Figure 5.3 Fabrication of the hybrid silica/polymer strain gauge: a) alignment of the two MMFs; b) polymer sensing element is fabricated between two MMFs

Analyzer Agilent 86142B), an optical circulator, a strain sensor, and an optical spectrum analyzer (OSA). The whitelight generated by the BBS is coupled into the optical fiber and is routed towards the strain gauge by the optical coupler. When the whitelight encounters the

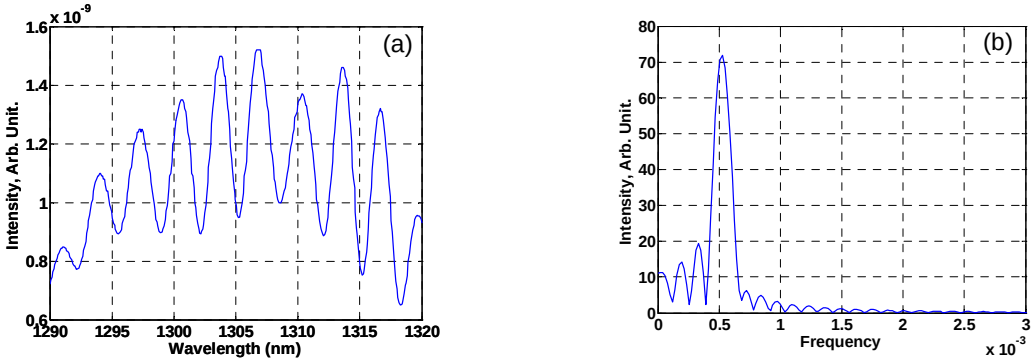

Figure 5.4 Reflectance fringe spectrum of a silica/polymer strain gauge and its FFT

strain sensor, a portion of the light is reflected by the tapered polymer sensing element. This reflected light propagates back toward the coupler and is partially routed towards the OSA by the coupler. The OSA is employed to measure the spectrum of the reflected white light.

In order to apply strain on the sensor, the alignment setup shown in Figure 3.2 is used. The fiber mounted on the three axis translation stage was slowly pulled away. An image was taken at several stages with the help of the optical microscope. Using image processing techniques, the exact amount of strain applied on the sensing element was measured and compared with that calculated from the FFT of the fringe spectrum.

5.3. Testing Results

A fringe spectrum of the whitelight reflected by a typical hybrid silica/polymer strain sensor is shown in Figure 5.4.a. The peaks and the valleys, *i.e.* the fringes, in the spectrum are due to the interference of the two reflected beams. The spacing between the fringes is determined by the optical path difference (OPD) of the these two beams, which is a function of the distance between the two silica optical fibers. The OPD can be calculated by taking (FFT) of the fringe spectrum and identifying the peak frequency of the FFT spectrum (see Figure 5.4 b).

The micrographic images of the polymer sensing element under different strain levels are shown in Figure 5.5. Digital image processing software was utilized to measure the distance

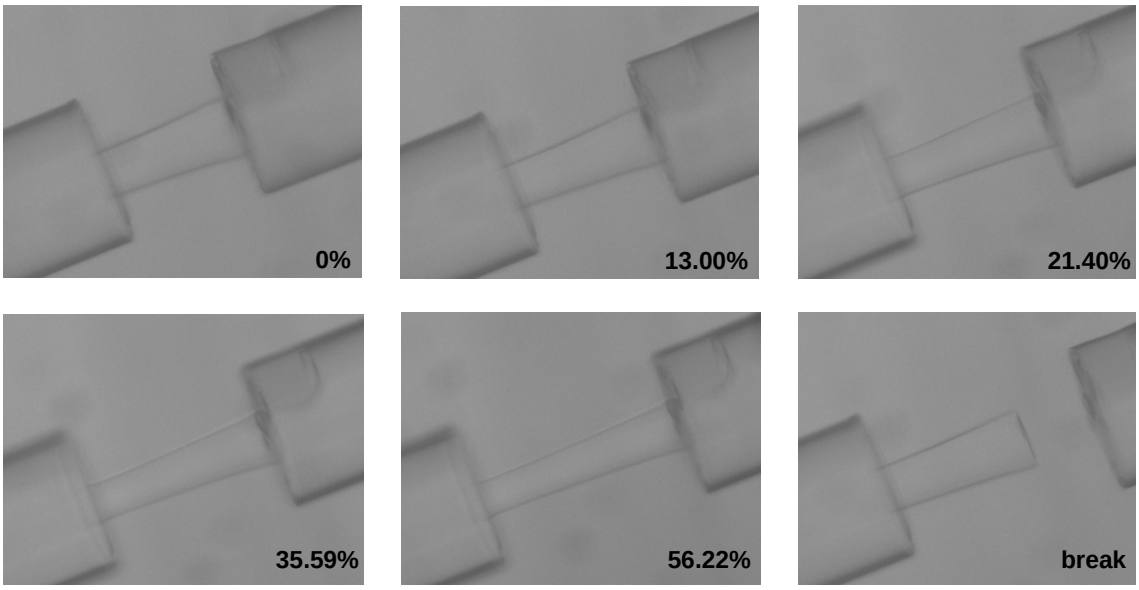

Figure 5.5 Micrographic images of the hybrid strain sensor under different strains

between the two silica optical fibers. The applied strains calculated from the elongations of the polymer sensing element are compared with the shifts of the FFT peak frequencies in Figure 5.6. A good linearity between the frequency shift and the applied strain was achieved. The strain sensor maintained its integrity under an applied strain as large as 56%.

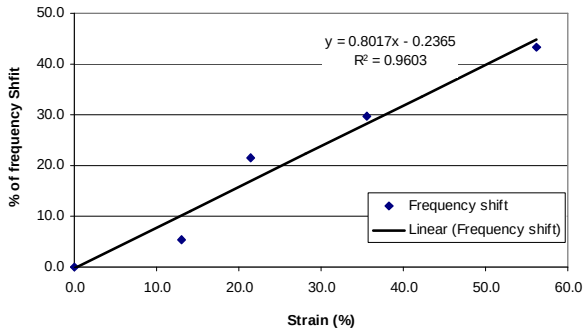

Figure 5.6 Linear relationship between frequency shift and applied strain

5.4. Conclusion

A strain sensor capable of measuring large strain was developed and its performance was evaluated. The applied strain was measured based on the FFT of the interference pattern obtained and was verified by image processing. It was observed that the sensor was capable of withstanding strain as large as 56%.

CHAPTER 6

FUTURE WORK

The objective of the work described in this thesis was to develop three optical fibers sensors to measure three physical parameters: distance, refractive index, and strain. This chapter discusses the future work to make these sensors commercially viable.

The polymer tip based distance sensor is clearly a better solution than the LPFG based distance sensor to measure arbitrary small distances. This advantage has great application in Near-Field Surface Profiling of samples. As discussed in Chapter 1, currently this is achieved by using a NSOM which involves placing a tapered probe in the near field of the sample so as to overcome the diffraction limit of conventional optical microscopes, thus achieving a lateral resolution of tens of nanometer in order for Near-Field surface profiling. Therefore the performance of the polymer tip based distance sensor needs to be evaluated on that scale. The probes used for such purposes have a nano-size aperture which is produced by either heating (with a CO_2 laser) and pulling [30] or by chemical etching. Chemical etching is the more popular approach since it allows for a much shorter cone and much larger angle [31]. Etching the optical fiber with an acrylate jacket on or applying a bevel to the etched fiber has resulted in smoother surfaces and the ability to produce various cone angles [32,33]. Most of these etching techniques have been developed for silica optical fibers. Therefore techniques that etch the polymer tip to achieve a desired aperture are needed to be studied in the future in order to manufacture the probe at the end of the optical fiber with the desired aperture and use it for Near-Field Profiling.

The refractive index sensor can be designed based on the sensitivity and measurement range required. Note that the length of the polymer core as well as its refractive index determine the sensitivity and the performance of the sensor. The spectral shift of the fringe position with

respect to the external refractive index is shown in Figure 6.1. The curve is non-linear for a large range but is piecewise linear over small regions i.e., n_{ext}=1.0~1.2, 1.2~1.3, 1.35-1.45 and 1.47-

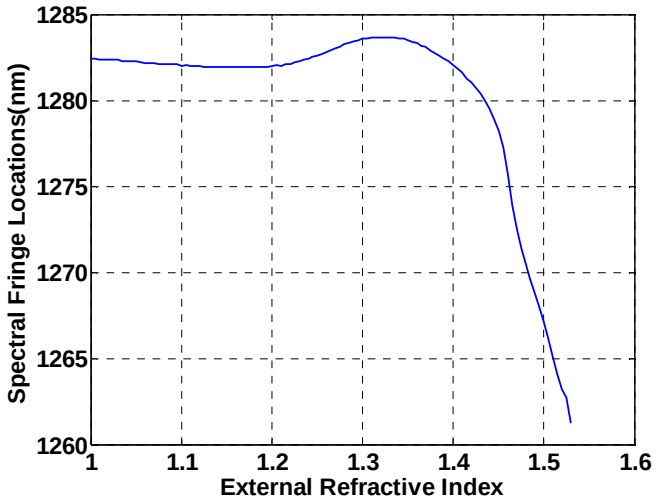

Figure 6.1 Variation of spectral fringe location with external refractive index when a broadband source with a central wavelength of 1310nm is used.

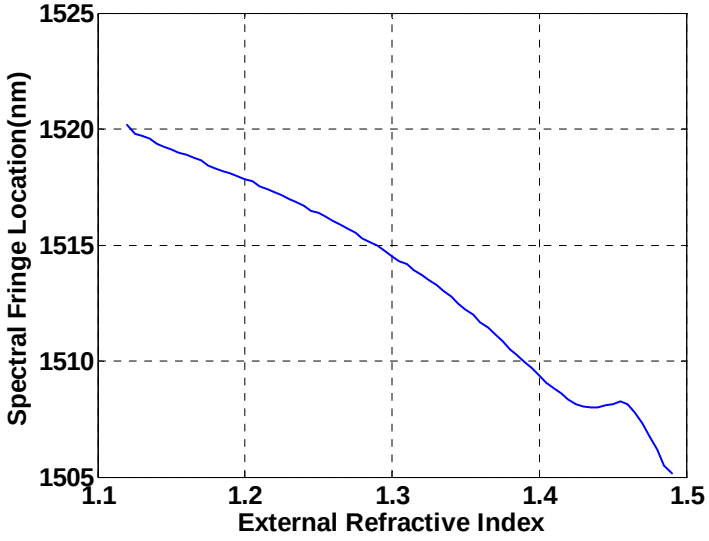

Figure 6.2 Variation of spectral fringe location with external refractive index when a broadband source with a central wavelength of 1550nm is used.

1.52 with each region having a different sensitivity. The non-linear behavior of the sensor is also dependent on the wavelength of the broadband source used (see Figure 6.2). Therefore a more detailed parametric study needs to be done on the performance of the sensor.

Large strain sensors find application in crack monitoring in concrete structures. Embedding an optical fiber inside the concrete helps in monitoring deep embedded cracks and also provides for better resolution of cracks due to the small dimensions of the fiber. The strain sensor developed can measure strain up to 56% and uses a simple low-cost manufacturing technique. Thus it would be ideal for use in monitoring cracks in concrete structures. For this purpose the sensor needs to be tested on real life specimens and a suitable packaging technique needs to be developed in order for it to be commercially viable.

The polymer tip based optical fiber sensor can also be used to measure temperature and distance simultaneously due to the introduction of an additional interferometric cavity, which seves as a reference fringe spectrum for either temperature or distance measurement. Further work on evaluating the polymer tip based optical fiber sensor for this purpose should be carried out.

APPENDIX A

MATLAB® FILE FOR DATA PROCESSING

```
function [xfilt,Rfilt,f,G]=f_fft1(lambda,R)
% data processing
n2=1.0; % external refractive index
fmax=2*n2*1000e-6; % assume maximum distance is 1mm
fs=fmax*10;  %sampling rate
dx=1/fs;
[x1, R1]=f_kxi_convert(lambda, R);  % R is sampled at kxi
plot(x1, R1); title('measured signal in wave number');
fs=1./mean(diff(x1)) % sampling frequency
Nfir=100; % order of the filter
Wn=[100e-6 2000e-6]/(fs/2) % range of the bandpass filter
[xfilt, Rfilt, R0]=f_fir_correct(x1, R1, Nfir, Wn,'b'); % applying the filter
figure; plot(xfilt, Rfilt); title('filtered signal');
w=hann(length(Rfilt)); % hanning window
Rfilt=Rfilt.*w;
[f, G]=f_fft_fk(Rfilt, fs, 2048*8); % FFT of the signal
figure; plot(f, G); title('fft');grid on;


function [kxi0, R0]=f_kxi_convert(lambda, R)
% function kxi_convert
% convert displayment of the fringe pattern on kxi=1/lambda
[Mr, Nr]=size(R);
if Mr==1
   lambda=reshape(lambda, Nr, Mr);
   R=reshape(R, Nr, Mr);
end
```

```
kxi=flipud(1./lambda);
R=flipud(R);
n2=1;
fmax=2*n2*1000e-6; % assume maximum distance is 1mm
fs=fmax*10;  %sampling rate
dx=1/fs;
kxi_min=min(kxi);
kxi_max=max(kxi);
kxi0=[kxi_min:dx:kxi_max].';  % sampling points along kxi
N=length(kxi0);
R0(1)=R(1);
R0(N)=R(Nr);
for ii=2:N-1
   index=find(kxi<kxi0(ii));
   p_l=index(length(index));
   kxi_l=kxi(p_l);
   index=find(kxi>kxi0(ii));
   p_h=index(1);
   kxi_h=kxi(p_h);
   R0(ii)=R(p_l)+(kxi0(ii)-kxi_l)/(kxi_h-kxi_l)*(R(p_h)-R(p_l));
end
R0=R0.';

function [tfilt, Rfilt, R0]=f_fir_correct(t, R, Nfilt, Wn, FilterType)
% filter the signal with a fir filter and compensate the time delay
% Inputs:
```

```
%   t: time
%   R: signal
%   Nfilt: order of the filter
%   Wn: cut-off frequency as defined by fir1
%   FilterType:
%       ='l', low pass
%       ='h', high pass
%       ='b', band pass
% Outputs:
%   tfilt: corrected time
%   Rfilt: filtered signal
%   R0: original signal at tfilt
NR=length(R);
Delay=Nfilt/2;
if FilterType=='h'
   filtB=fir1(Nfilt, Wn, 'h');
else
   filtB=fir1(Nfilt, Wn);
   %filtB=fir1(Nfilt, Wn, kaiser(Nfilt+1, -50));
   %filtB=fir1(Nfilt, Wn, Bartlett(Nfilt+1));
end
figure; freqz(filtB, 1, 1000);
Rf=filter(filtB, 1, R);  % filter
%figure; plot(t, R, t, Rf, 'r');
Rfilt=Rf((Delay+1+Nfilt):NR);
tfilt=t(Nfilt+1:NR-Delay);
```

```
R0=R(Nfilt+1:NR-Delay);
return


function [fk, Rfft]=f_fft_fk(R, fs, Nfft)
% find the FFT of R as a function of frequency fk
% Inputs:
%    R: signal
%    fs: sampling frequency
%    Nfft: # of fft
% Outputs:
%    fk: frequency
%    Rfft: real value of fft(R)
Rfft=abs(fft(R, Nfft));  % fft of signal R
Rfft=Rfft(1:floor(Nfft/2));
fk=fs*[0:floor(Nfft/2)-1]/Nfft;
```

APPENDIX B

MATLAB® FILE FOR POLYMER TIP SIMULATION

```
function [sum1,sum2,D]=beta_sumz(lambda,ref)
% Simulation of the reflectance spectrum of the Polymer tip for a particular wavelength
% lambda- wavelength (nm)
% ref - external refractive index
sum1=0;
sum11=0;
sum2=0;
n0=1.56; % refractive index of the polymer core
k=(2*pi)/lambda;

% determining the roots of the bessel function
J0=besselj(0,[0:0.01:20]);
J=J0(1:length(J0)-1).*J0(2:length(J0));
index=find(J<=0);
U=index(2:length(index))./100;

% V-number
V1=2*pi*4e-6*sqrt(n0^2-ref^2)/lambda;

% phase due to the fundamental mode
u=2.404*exp(-1/V1);
delta=(n0^2-ref^2)/n0^2;
beta=sqrt(k^2*n0^2-(u/4e-6)^2);
ne=beta/k;
D=(2*pi*((ne*72e-6)/lambda));
```

```
% phase due to polymer core considering the higher modes
for(t=1:1:length(U))
   sum2(t)=0;
   u=U(t)*exp(-1/V1);
   sum11=(exp(-2/V1)*((U(t)^2-2.404^2)/(2*k*(4e-6)^2*n0)));
   sum2(t)=sum11;
   % sum of both phases.
   sum1=sum1+cos((sum11*72e-6)+D);
end
```

APPENDIX C

PROPERTIES OF NORLAND OPTICAL ADHESIVE 61

Typical Properties of NOA 61	
Solids	100%
Viscosity at 25° C	300 cps
Refractive Index of Cured Polymer	1.56
Elongation at Failure	38%
Modulus of Elasticity (psi)	150,000
Tensile Strength (psi)	3,000
Hardness - Shore D	85

Available at <http://www.norlandprod.com/adhesives/NOA%2061.html>

APPENDIX D

NICHIA NSHU550A DATA SHEET

1.SPECIFICATIONS

(1) Absolute Maximum Ratings (Ta=25°C)

Item	Symbol	Absolute Maximum Rating	Unit
Forward Current	I_F	25	mA
Pulse Forward Current	I_{FP}	80	mA
Allowable Reverse Current	I_R	85	mA
Power Dissipation	P_D	100	mW
Operating Temperature	T_{opr}	-30 ~ + 85	°C
Storage Temperature	T_{stg}	-40 ~ +100	°C
Soldering Temperature	T_{sld}	265°C for 10sec.	

I_{FP} Conditions : Pulse Width ≦ 10msec. and Duty ≦ 1/10

(2) Initial Electrical/Optical Characteristics (Ta=25°C)

Item		Symbol	Condition	Min.	Typ.	Max.	Unit
Forward Voltage		V_F	I_F=20[mA]	-	3.5	4.0	V
Peak Wavelength		λ_P	I_F=20[mA]	370	375	380	nm
Spectrum Half Width		$\triangle\lambda$	I_F=20[mA]	-	10	-	nm
Optical Power Output	Rank 3	P_o	I_F=20[mA]	1200	1400	1700	μW
	Rank 4	P_o	I_F=20[mA]	1700	2000	2400	μW
	Rank 5	P_o	I_F=20[mA]	2400	2800	3400	μW

* Optical Power Output Measurement allowance is ±10%.

** Peak Wavelength Measurement allowance is ±3nm.

*** One delivery will include up to three different ranks of the products.
The quantity-ratio of the three ranks is decided by Nichia.

2.TYPICAL INITIAL OPTICAL/ELECTRICAL CHARACTERISTICS

Please refer to figure's page.

3.OUTLINE DIMENSIONS AND MATERIALS

Please refer to figure's page.

Material as follows ; Glass : Hard Glass
Cap : Ni Plating Iron Alloy
Lead : Au Plating Iron Alloy

Available at < http://www.nichia.com/specification/led_lamp/NSHU550A-E.pdf>

REFERENCES

1. Caldas, P., *et al.*, *Modal LPG-based mach-zehnder interferometer with controlled sensitivity for refractive index measurement,* Proc. SPIE, Vol. 7004, 2008, pp. 700448.
2. Majumdar, A., Huang, H., *Development of an in-fiber whitelight interferometric distance sensor for absolute measurement of arbitrary small distances,* App. Opt., Vol. 47 No.15, May 2008, pp. 2821-2828.
3. Jianshu, L., Zhong, X., *Study on optical fiber concentration sensor,* Proc. SPIE, Vol. 1319, 1990, pp. 512-513.
4. Barian, C., *et.al., Optical fiber humidity sensor based on a tapered fiber coated with agarose gel,* Sens. and Act. B, Vol. 69, 2000, pp.127-131.
5. *Glass Photosensitivity and Fiber Gratings*, Fiber Optics Research Center GPI RAN, 2003-04.

   Available at: < http://gratings.fo.gpi.ru/index.php?page=11> as on 10/6/2008.
6. Lee, D.C., *et al., Monitoring of fatigue damage of composite structures by using embedded intensity-based optical fiber sensor,* Smart Mat & Struc., Vol. 10, 2001, pp. 285-292.
7. Pinet, E., Cibula, E., Denis, D., *Ultra miniature all-glass fabry-perot pressure sensor manufactured at the tip of a multimode fiber,* Proc. SPIE, Vol. 6770, 2007, pp. 67700U.
8. Jiang, S., *et al., Optical fiber sensor for tensile and compressive strain measurement by white-light fabry-perot interferometry,* Opt. Engg, Vol. 46(3), March 2007, pp. 034402.
9. Dunn, R., *Near-field scanning optical microscopy,* Chem. Rev., Vol. 99,1999, pp.2891-2927.
10. Shiku, H., *et al., Non-contact near-field scanning optical microscopy imaging using an interferometric optical feedback mechanism,* Langmuir, Vol. 15, 1999, pp. 2162-2168.

11. James, S.W., Tatam R.P., *Optical fiber long period fiber bragg grating sensors: characteristics and application,* Meas. Sci. & Tech., Vol. 14, 2003. pp. R49-R61.
12. Yokouchi, T., *et al., Thermal tuning of mechanically induced long-period fiber grating,* App. Opt., Vol 44 no. 24, August 2005, pp. 5024-5028.
13. Lacroix, S., *et al.*, *Tapered monomode optical fibers: understanding large power transfer*, App.Opt., Vol. 25, 1986, pp. 4421-4425.
14. Allsop, T., et al., A high sensitivity refractometer based upon a long period grating Mach-Zehnder interferometer, Rev. Sci. Instrum., Vol. 73, 2002, pp. 1702-1705 .
15. Patrick, H.J, Kersey A.D., and Bucholtz F., *Analysis of the response of long period fiber gratings to external index of refraction*, J. Lightwave Tech., Vol. 16, 1998, pp. 1606-1612.
16. Iadicicco, A., *et al.*, *Thinned fiber bragg gratings as refractive index sensors*, IEEE Sens. J. Vol. 5, 2005, pp. 1288-1295 .
17. Iadicicco, A., *et al.*, *Refractive Index Sensor based on microstructured fiber bragg grating*, IEEE Phot. Tech. Lett. , Vol. 17, 2005, pp. 1250-1252.
18. Culshaw, B., *et al.*, *Evanscent wave methane detection using optical fibers*, Electron. Lett., Vol. 28, 1992, pp. 2232-2234.
19. Cox, F.M., Lwin, R., Large, M.C.J., and Cordeiro, C.M.B., *Opening up optical fibres*, Opt. Exp., Vol. 15, 2007, pp. 11843-18848.
20. Newby, K., Reichart, W.M., Andrade, J.D., and Benner, R.E., *Remote spectroscopic sensing of chemical absorption using a single multimode optical fiber*, App. Opt. , Vol. 23, 1984, pp. 1812-1815.
21. Snyder, A.W.,*Coupling of modes on a tapered dielectric cylinder*, IEEE Trans. Micro.Th. and Tech., Vol. MTT-18, 1970, pp. 383-392.
22. Cassidy, D.T., Johnson, D.C., and Hill, K.O., *Wavelength-dependent transmission of monomode optical fiber tapers*, App. Opt., Vol. 24, 1985, pp. 945-950.

23. Ding, J., *et al.*, *Fiber-taper seeded long-period grating pair as a highly sensitive refractive-index sensor*, IEEE Phot. Tech. Lett., Vol. 17, 2005, pp. 1247-1249.

24. Tian, Z., Yam, S.S-H., and Loock, H., *Refractive index sensor based on abrupt taper Michelson interferometer in a single-mode fiber*, Opt. Lett., Vol. 33, 2008, pp. 1105-1107.

25. Ansari, F., *Fiber optic health monitoring of civil structures using long gage and acoustic sensors*, Smart Materials and Structures, Vol. 14, pp. S1-S7.

26. Friebele, E. *et al.,Optical Fiber sensors for spacecraft applications*, Smart Materials and Structures, Vol. 8, 1999, pp. 813-838.

27. Zhou, G. and Sim, L., *Damage detection and assessment in fiber-reinforced composite structures with embedded fiber optic sensors – review*, Smart Materials and Structures, Vol. 11,2002, pp. 925-939.

28. Kiesel, S. *et al., Polymer optical fiber sensors for civil infrastructure*, Proc. of SPIE, Vol. 6174, 2006, pp. 617435-1.

29. Kuang, K. *et al.*, *An evaluation of a novel plastic optical fibre sensor for axial strain and bend measurements*, Measurement Science and Technology, Vol. 13, 2002, pp.1523-1534.

30. Valaskovic, G.A., Holton, M., Morrison, G.H*., Biological near-field scanning optical microscopy: instrumentation and sample issues for shear-force feedback*, Ultramicroscopy, Vol. 57 no.2-3, Feb 1995, pp. 212-218.

31. Novotny, L., Pohl, D.W., Hecht, B., *Scanning near-field optical probe with ultrasmall spot size*, Vol. 20 no.9, May 1995, pp. 970.

32. Lambelet, P., *et al., Chemically etched fiber tips for near-field optical microscopy: a process for smoother tips*, App. Opt., Vol. 37 no.31., Nov.1998, pp. 7289.

33. Held, T., *et al., Method to produce high-resolution scanning near-field optical microscope probes by beveling optical fibers*, Vol. 71 no.8, Aug. 2000, pp. 3118.

BIOGRAPHICAL INFORMATION

Ayan is currently pursuing a Master's degree in Mechanical Engineering at the University of Texas at Arlington. His research interests include Optical fiber sensors, Finite Element Analysis and Structural Health Monitoring. He has been a Graduate Research Assistant in the Advanced Sensor Technology lab at the University of Texas at Arlington since January 2007. He enjoys playing chess and cricket.